Two volcanic tsunami events caused by trapdoor faulting at a submerged caldera near Curtis and Cheeseman Islands in the Kermadec Arc

Osamu Sandanbata[1], Shingo Watada[2], Kenji Satake[2], Hiroo Kanamori[3], and Luis Rivera[4]

[1]National Research Institute for Earth Science and Disaster Resilience
[2]University of Tokyo
[3]Seismological Laboratory, California Institute of Technology
[4]Université de Strasbourg

November 22, 2022

Abstract

Two unusual submarine earthquakes (Mw 5.8) occurred near volcanic islands, called Curtis and Cheeseman, in the Kermadec Arc in 2009 and 2017. Following both earthquakes, similar tsunamis with wave heights of about a meter, that are disproportionate to their moderate seismic magnitudes, were observed by coastal tide gauges. We investigate the source mechanism for both earthquakes by analyzing tsunami and seismic data of the 2017 event. Preliminary analysis of tsunami data indicates that the earthquake uplifted a submerged caldera around the islands. Source modeling using tsunami and seismic data reveals that a trapdoor faulting, involving ring-faulting and deformation of an underlying magma reservoir, occurred due to magma overpressure in the reservoir, possibly in association with caldera resurgence. The relationship between the maximum fault slip and the seismic magnitude for trapdoor faulting events found at global calderas is different from that for regular earthquakes, reflecting the peculiarity of the volcanic earthquakes.

Two volcanic tsunami events caused by trapdoor faulting at a submerged caldera near Curtis and Cheeseman Islands in the Kermadec Arc

Osamu Sandanbata[1,2,†], Shingo Watada[1], Kenji Satake[1], Hiroo Kanamori[3], and Luis Rivera[4]

[1] Earthquake Research Institute, the University of Tokyo, Tokyo, Japan.

[2] National Research Institute for Earth Science and Disaster Resilience, Ibaraki, Japan.

[3] Seismological Laboratory, California Institute of Technology, Pasadena, CA, USA.

[4] Université de Strasbourg, CNRS, ITES UMR 7063, Strasbourg F-67084, France.

Corresponding author: Osamu Sandanbata (osm3@bosai.go.jp)

†*Now at* National Research Institute for Earth Science and Disaster Resilience, Ibaraki, Japan.

Key Points:

- Unusual tsunamis were caused by two M_w 5.8 volcanic earthquakes in 2009 and 2017 near Curtis and Cheeseman Islands in the Kermadec Arc.
- By analyzing tsunami and seismic data of the 2017 event, we suggest that the trapdoor faulting occurred at a submerged resurgent caldera.
- Trapdoor faulting events recently found at global calderas had abnormally large fault slips, implying their atypical earthquake physics.

Abstract

Two unusual submarine earthquakes (M_w 5.8) occurred near volcanic islands, called Curtis and Cheeseman, in the Kermadec Arc in 2009 and 2017. Following both earthquakes, similar tsunamis with wave heights of about a meter, that are disproportionate to their moderate seismic magnitudes, were observed by coastal tide gauges. We investigate the source mechanism for both earthquakes by analyzing tsunami and seismic data of the 2017 event. Preliminary analysis of tsunami data indicates that the earthquake uplifted a submerged caldera around the islands. Source modeling using tsunami and seismic data reveals that a *trapdoor faulting*, involving ring-faulting and deformation of an underlying magma reservoir, occurred due to magma overpressure in the reservoir, possibly in association with caldera resurgence. The relationship between the maximum fault slip and the seismic magnitude for trapdoor faulting events found at global calderas is different from that for regular earthquakes, reflecting the peculiarity of the volcanic earthquakes.

Plain Language Summary

Most tsunamis are generated by large earthquakes with seismic magnitudes $M > \sim 7$, but two moderate-size earthquakes with only M 5.8 near volcanic islands, north of New Zealand, generated unusual tsunamis with a maximum wave height of about a meter. In this study, we examine the unusual source mechanism of the volcanic earthquakes that cause disproportionate tsunamis. By analyzing the records of tsunamis and seismic waves from the earthquakes, we suggest that the inside of a curved fault system beneath a submerged volcano with a caldera structure suddenly moved upward, together with a volume increase of a shallow magma reservoir. Overpressure created by magma accumulation beneath the submarine caldera recurrently induces meter-scale tsunamis without significant ground motions, calling for attention to tsunami hazards from submarine calderas.

1 Introduction

On 17 February 2009 and 8 December 2017 (UTC), peculiar tsunamis were recorded at coastal tide gauges in New Zealand, after shallow earthquakes with moment magnitudes M_w 5.8. Both earthquakes occurred near Curtis and Cheeseman Islands, volcanic islands in the Kermadec Arc (Figure 1; Table S1), we hereafter call them *Curtis earthquakes*. The maximum tsunami wave heights from the 2009 and 2017 earthquakes were about 50 cm (LOTT) and 80 cm (RFRT), respectively (Figure 1c), which are much larger than expected for their moderate seismic magnitudes (Abe, 1981). The tsunami waveforms from these earthquakes were similar at three stations (LOTT, NCPT, and TAUT). Both earthquakes also showed similar moment tensors dominated by the compensated-linear-vector-dipole (CLVD) component with a nearly vertical tension-axis, which are types of *vertical-T CLVD earthquake* often observed at volcanoes (Sandanbata, Kanamori, et al., 2021; Shuler, Ekström, et al., 2013; Shuler, Nettles, et al., 2013). These observations imply that similar volcanic phenomena repeatedly occurred near the islands and caused unusual tsunamis.

The mechanism of such tsunamigenic vertical-T CLVD earthquakes has been controversial. For the Curtis earthquakes, Gusman et al. (2020) analyzed data of tsunami waveforms at tide gauges and broad-band (20–500 s) seismic waveforms at the global seismograph network (GSN) and proposed a mechanism involving two sources at different

depths. They suggested that a hydrofracturing source at ~1.5 km depth generated tsunamis without significant seismic radiations, and a deeper source at ~10 km related to fluid flow radiated seismic waves. Similar tsunamigenic vertical-T CLVD earthquakes were observed at Sumisu caldera, south of Japan, for which various mechanisms were proposed: hydrofracturing of magma-water interaction (Kanamori et al., 1993; Satake & Kanamori, 1991), ring-faulting (Ekström, 1994), shallow tensile crack (Fukao et al., 2018). Recently, Sandanbata et al. (2022) showed that the trapdoor faulting mechanism explains both tsunami and long-period seismic waveform data from the 2015 event at Sumisu caldera.

In this study, we investigate the source mechanism of the Curtis earthquakes using tsunami and seismic data from the 2017 earthquake by taking a similar approach as done by Sandanbata et al. (2022). We first use only the tsunami data to estimate the vertical sea-surface displacement due to the earthquake. We then explore a unified source model explaining both the tsunami and long-period seismic data. Finally, we propose a source mechanism and discuss possible submarine volcanism and an atypical scaling relationship for vertical-T CLVD earthquakes at global calderas.

2 Data

2.1 Tsunami data

We use four tsunami waveform data from the 2017 earthquake, recorded at four coastal tide gauges, RBCT, RFRT, LOTT, and GBIT, with a sampling rate of one sample/minute (Figure 1c). We extract the tsunami signals from the raw record by removing tidal trends approximated as low-order polynomial functions. The tsunami signals have dominant periods from 200 s to 500 s. We do not use the records of NCPT and TAUT, because of poor signal-to-noise ratios.

2.2 Long-period seismic data

We use long-period seismic waveform data from the 2017 earthquake, recorded on LH or BH channels at seismic stations (network codes: IU, NZ, AU, and G), downloaded from the Data Management Center of the Incorporated Research Institutions for Seismology (IRIS). We select 33 good-quality records after data screening, remove the instrument response from the seismograms to obtain displacement records, and apply a one-pass fourth-order Butterworth band-pass filter with corner frequencies at 0.005 and 0.0125 Hz (band-pass period: 80–200 s); these procedures are performed with the W-phase package (Duputel et al., 2012; Hayes et al., 2009; Kanamori & Rivera, 2008).

3 Vertical sea-surface displacement of the 2017 earthquake

We first estimate the vertical sea-surface displacement due to the 2017 earthquake using the tsunami data (see Text S1, for details). For the estimation, we first simulate dispersive tsunami waveforms at the tide gauges by the JAGURS code (Baba et al., 2015) and delay the synthetic waveforms at the two distant gauges, LOTT and GBIT, to approximately incorporate the effect of the seawater compressibility and the elastic Earth (Ho et al., 2017; Sandanbata, Watada, et al., 2021; Watada et al., 2014). We then perform a tsunami waveform inversion to reconstruct a vertical sea-surface displacement that reproduces the tsunami data.

The obtained model (Figure 2a) involves a large uplift of ~1.3 m localized in the southwest of the islands, a peripheral subsidence of ~1.3 m to the south of the uplift, and another meter-scale uplift located about 5 km away from the islands to the southeast. This model explains the tsunami waveform data well (Figure 2b). To examine the robustness of the model, we also estimate a sea-surface *uplift* model without subsidence by imposing the non-negative condition on the inversion. In the obtained uplift model (Figure 2c), a localized uplift is estimated similarly to the southwest of the islands but with a larger maximum amplitude of ~2.4 m. In this case, the uplift to the southeast of the islands seen in Figure 2a disappears. Despite the model differences, the tsunami waveform fit of the uplift model is comparable to that of the model with both uplift and subsidence (compare Figures 2b and 2d). These results suggest that the tsunami was excited mainly by the uplift localized at the southwest of the islands, while the peripheral sources are not resolved well and could be artifacts due to the low sampling rate and the limited azimuthal coverage of the tsunami waveform data.

4 Source modeling of the 2017 earthquake

To find a plausible source mechanism, we compare the localized uplift with the submerged structure (Figure 3a). Curtis and Cheeseman Islands are on top of a cone structure surrounded by bathymetric depression, indicating a submerged caldera with a size of 7 km × 6 km. The existence of the caldera was mentioned in a volcano catalogue (Global Volcanism Program, 2013), which we hereafter call *Curtis caldera*. As compared in Figure 3a, the sea-surface displacement we estimated is localized over the southwest of the caldera, suggesting that the earthquake caused an asymmetric uplift of the submerged caldera.

Given the caldera deformation pattern, *trapdoor faulting* (Figure 3b) would be a good candidate for the source mechanism. This mechanism, driven by magma overpressure in a shallow reservoir, was first proposed for earthquakes at a subaerial caldera of Sierra Negra volcano, Galapagos (Amelung et al., 2000), and recently found at Sumisu caldera (Sandanbata et al., 2022). These previous studies showed that a trapdoor faulting causes a large asymmetric caldera-floor uplift with a vertical-T CLVD earthquake, like observations for the 2017 Curtis earthquake. Doyle et al. (1979) reported long-term uplift and fumaroles on/around Curtis Island, implying recent magma supply into a reservoir beneath the caldera that would have the potential for generating trapdoor faulting.

Considering the mechanism, we explore an earthquake source model by using both the tsunami and long-period seismic data. We follow the methodology of Sandanbata et al. (2022), as summarized here briefly (see Text S2, for details). First, we assume a fault-crack composite source system, or an inward-dipping partial ring fault connected to a horizontal crack at a depth of 3 km (see triangular meshes shown in Figures 3c and S1). We fix a partial ring fault on the southwestern side of the caldera (Figure 3c), given the localized uplift over the southwestern caldera floor (Figure 3a), but vary the dip angle of the ring fault. Second, we perform a tsunami waveform inversion to determine amounts of the reverse slip of the ring fault and the vertical opening/closure of the horizontal crack; here, we assume that the vertical component of the ring-fault slip at the bottom is similar to the opening amount of the horizontal crack at its contact. Thus, we obtain source models explaining the tsunami data. Third, we compute long-period (80–200 s) seismograms from the source models and compare them with the seismic data for validation.

Consequently, we find a source model that explains the tsunami and long-period seismic data. First, the tsunami waveform inversion successfully determines the motions of the fault-crack composite source system. An example model, shown in Figure 3c, is expected to displace the sea surface vertically by ~2 m (Figure 4a), which reproduces the observed tsunami waveform overall (Figure 4b). Although we vary the dip angle of the ring fault, all the obtained models similarly explain the tsunami data (Figure S2) and yield small misfit values (tsunami NRMS of 0.60–0.76; Figure 3d). This indicates weak constraints on the ring-fault dip angle from the tsunami data. Note that, when we assume that a horizontal crack lies at a deeper depth of 6 km, the inversion still gives a small misfit (NRMS of 0.77; Figure S3), implying the difficulty in determining from the data how deep the source system extends.

In contrast, long-period seismic wave amplitudes from the tsunami-based models with a crack at a depth of 3 km change largely depending on the ring-fault dip angle (Figure S4), resulting in large variations of the misfit of seismic waveforms (seismic RMS of 0.86–2.08 μm; Figure 3d). This is because the seismic radiation of a shallow ring-faulting becomes less efficient as the dip is close to vertical (Sandanbata, Kanamori, et al., 2021). Thus, models with dip angles in a narrow range of 75° to 80° yield reasonable fits to the seismic data (Figure 3d). Figures 4c–e shows moment tensors and long-period seismograms computed from the model shown in Figure 3c, which has a ring-fault dip angle of 78°; this model explains the seismic waveform data well, yielding the smallest misfit (Figure 3d).

Therefore, we propose the model shown in Figure 3c as a best-fit source model. This model has a reverse slip of 4.4 m at a maximum along a ring fault with a dip angle of 78° and asymmetric opening and closure of the horizontal crack at a depth of 3 km with maximum amounts of 5.4 m and 2.9 m, respectively. The crack increases its inner volume by $+3.5 \times 10^7$ m^3. This model causes a sea-surface uplift localized over the southwestern caldera with smaller subsidence outside of the fault (Figure 4a). The pattern and amplitude of this sea-surface displacement are different from those estimated in Section 3 (Figures 2a and 2c) due to strong constraints from the fault-crack source system, but this model explains the tsunami data reasonably well (Figure 4b). Figure S5 shows synthetic tsunami waveforms from the horizontal crack and the ring fault separately, demonstrating that both parts contribute the tsunami generation.

The moment tensor computed from the model is highly isotropic with M_w 6.24 (Figure 4c; Table S4), composed of a horizontal crack (M_w 6.19) with a strong isotropic component and a ring fault (M_w 5.96) with a large vertical-T CLVD component (Figure 4d). In Figure S6, we show that only limited components of the ring fault, which constitute a vertical-T CLVD moment tensor, mainly contribute to the seismic radiation, and that the horizontal crack contributes little (see Text S3, for details). This explains why vertical-T CLVD moment tensors were obtained by moment tensor analyses assuming no isotropic component, as seen in the GCMT catalogue.

5 Discussion & Conclusions

5.1 Trapdoor faulting mechanism

We have shown that the fault-crack composite source model (Figure 3c) can explain both the tsunami and long-period seismic data from the 2017 Curtis earthquake. The

asymmetrical motion of the fault-crack composite source system shown by our model is similar to those estimated for trapdoor faulting events at Sumisu and Sierra Negra calderas (Sandanbata et al., 2022; Zheng et al., 2022). Hence, following interpretations of these previous studies, we suggest that the trapdoor faulting occurred at Curtis caldera in the following scenario; the reverse slip initially took place on the southwestern ring fault due to overpressure of magma accumulating in the horizontal crack, and the upper wall of the horizontal crack near the fault moved up; the resultant crack volume increase successively depressurized the inner magma, causing the downward motion of the upper wall of the crack on the other side. Our model showed atypical source properties: large slip of several meters along the ring fault, shallow source depth near the seafloor, and fault-reservoir composite source. These characteristics explain the efficient tsunami generation without significant seismic radiation, as Sandanbata et al. (2022) revealed for events at Sumisu caldera.

Given similarities between the two (2009 and 2017) Curtis earthquakes, we suggest that the trapdoor faulting recurred at the submerged caldera. The tsunami waveforms of the two earthquakes are almost identical at three tide gauges, LOTT, NCPT, and TAUT (Figure 1c); as Gusman et al. (2020) showed, the spectra of the tsunami waveforms from the two earthquakes are very similar. To further investigate the similarity of the earthquakes, we perform deviatoric moment tensor analysis using long-period seismic data (see Text S4). Since the two moment tensor elements, $M_{r\theta}$ and $M_{r\varphi}$, are indeterminate for such shallow earthquakes, we remove the two elements and obtain *resolvable moment tensors* $\boldsymbol{M_{res}}$ (Sandanbata, Kanamori, et al., 2021) (Figure S7). Following relationships between $\boldsymbol{M_{res}}$ and the ring-fault geometry (Sandanbata, Kanamori, et al., 2021), similar null-axis directions (NNW-SSE) of the two $\boldsymbol{M_{res}}$ indicate that their ring-fault segments are oriented similarly, while a more dominant vertical-CLVD component (larger k_{CLVD}; see the definition in Text S4) for the 2017 earthquake implies a larger ring-fault arc angle compared to that of the 2009 earthquake. Recurrence of similar trapdoor faulting was reported for Sumisu and Sierra Negra calderas, being attributed to continuous magma supply beneath the calderas until the initiation of ring-faulting (Gregg et al., 2022; Bell, Hernandez, et al., 2021; Bell, La Femina, et al., 2021; Sandanbata et al., 2022); this would be the case for Curtis caldera.

Gusman et al. (2020) proposed a different mechanism for the Curtis earthquakes to explain datasets of tsunami and broadband seismic waveforms. They separately attributed the tsunami generation to a hydrofracturing source at a shallow depth and the vertical-T CLVD seismic radiation to a deeper source. On the other hand, we showed that a trapdoor faulting within the caldera, involving ring-faulting and sill-like reservoir deformation at a shallow depth, reproduced the tsunami and long-period seismic waveforms. Tsunami waveforms expected for the two mechanisms seem indistinguishable from the available tide-gauge data. Also, given the difficulty in determining source depths of shallow seismic sources (Ekström et al., 2012) and the complexity of seismic sources involving volume changes (Kawakatsu et al., 1996), it should be challenging to distinguish these two different mechanisms from available regional- to far-field seismic data.

5.2 Implications for submarine volcanism

The trapdoor faulting events may have occurred in the *resurgence* process of Curtis caldera. The resurgence is a long-term caldera uplift driven by gradual pressure increase of magma accumulating in a shallow reservoir and facilitated by reactivations of ring faults, which have been observed at many calderas like Toba, Long Volley, Valles, and Iwo-Jima

(Ioto). Although most resurgent calderas accompany only small earthquakes with $M < \sim 3$ (Acocella et al., 2015; references therein), trapdoor faulting events of $M \sim 5$ were reported during the resurgence of Sierra Negra caldera (Bell, Hernandez, et al., 2021; Bell, La Femina, et al., 2021; Gregg et al., 2018, 2022; Jónsson, 2009). Previous surveys near Curtis caldera suggest the caldera resurgence in the past. Doyle et al. (1979) conducted bathymetry surveys and the radiocarbon dating of barnacles on the islands and found that long-term uplift, as large as ~7 m from 1929 to 1964, and ~18 m during about 200 years, took place in this area. The cone structure within the caldera (Figure 3a) is possibly a *resurgent dome*; such structures are seen within many resurgent calderas (Acocella, 2019; Acocella et al., 2001) and replicated by numerical/analogue models (Acocella & Funiciello, 1999; Brothelande et al., 2016). Also, active fumaroles found on the island at the dome summit (Doyle et al., 1979) are common for resurgent domes (Cole et al., 2005; Molin et al., 2003).

The direct relationship between trapdoor faulting and submarine eruptions at Curtis caldera remains unclear. About a month before the 2009 earthquake, ocean acoustic waves that originated from near the caldera were recorded by a seismic network (Global Volcanism Program, 2013). These signals may have indicated submarine eruptions, but their origins are yet to be confirmed. Further investigations of the caldera using ocean acoustic signals, *in-situ* observations, or bathymetric surveys will help us understand submarine volcanism of the caldera.

5.3 Earthquake scaling relationship for trapdoor faulting

Recent observations of trapdoor faulting suggest that it has an earthquake scaling relationship that is distinct from those for tectonic earthquakes. Figure 5 shows the seismic magnitude and the maximum slip on the intra-caldera fault of source models proposed for trapdoor faulting events at three calderas: the 2017 event at Curtis (M_w 5.8 and 4.4 m; this study), the 2015 event at Sumisu (M_w 5.7 and 6.8 m, Sandanbata et al. [2022]), and the 2005 event at Sierra Negra (m_b 4.6 and 2.0 m; Zheng et al. [2022]; we use m_b because M_w was not reported). Compared with the empirical scaling relationship by Wells & Coppersmith (1994), the trapdoor faulting events contained far larger, 10–20 times, maximum slip than those for tectonic earthquakes with similar magnitudes, reflecting their atypical earthquake physics. Shuler et al. (2013) reported that vertical-CLVD volcanic earthquakes, including some of the events at Sumisu and Curtis calderas, have longer source durations compared to the global average for similar-sized earthquakes. These peculiarities may arise from such mechanism as a fault system connected to the reservoir void, a shallow source depth, and local stress created by magma overpressure, and/or rock-fluid interaction (Sandanbata et al., 2022). For better understanding, the dynamics of interactive fault-reservoir source systems at calderas needs to be explored.

Acknowledgments

The authors thank Zhongwen Zhan for helpful discussion. This study is funded by the JSPS KAKENHI (Grant numbers: JP17J02919, JP20J01689, and JP19K04034), by the JST J-RAPID (JPMJJR1805). Osamu Sandanbata's travel to California Institute of Technology was supported by Oversea Internship Program of Earthquake Research Institute, the University of Tokyo.

Data availability

The tide-gauge data are provided from Land Information New Zealand (LINZ; https://www.linz.govt.nz/sea/tides/sea-level-data/sea-level-data-downloads). The topography and bathymetry data are provided from GEBCO Compilation Group through the British Oceanographic Data Centre (Weatherall et al., 2015; https://www.gebco.net/data_and_products/gridded_bathymetry_data/gebco_30_second_grid/), the National Institute of Water and Atmospheric Research in New Zealand (NIWA; https://niwa.co.nz/our-science/oceans/bathymetry), and LINZ (https://data.linz.govt.nz/). The seismic data are available through the IRIS Wilber 3 system (https://ds.iris.edu/wilber3/) or IRIS Web Services (https://service.iris.edu/), including the seismic networks of IU (GSN; Albuquerque Seismological Laboratory, 1988), AU (ANSN; H., G., & Geoscience Australia, 2021), NZ (New Zealand National Seismograph Network), and G (GEOSCOPE; IPGP & EOST, 1982). The earthquake information is available from the GCMT catalogue (Ekström et al., 2012; https://www.globalcmt.org/https://www.globalcmt.org/). The W-phase package (Duputel et al., 2012; Hayes et al., 2009; Kanamori & Rivera, 2008) is available through the website of W Phase source inversion (http://eost.u-strasbg.fr/wphase/index.html). We plotted focal mechanisms representing moment tensors with a MATLAB code developed by James Conder (available from https://www.mathworks.com/matlabcentral/fileexchange/61227-focalmech-fm-centerx-centery-diam-varargin). The best-fit source model presented in this paper is contained in Data Set S1.

304 **References**

305 Abe, K. (1981). Physical size of tsunamigenic earthquakes of the northwestern Pacific. *Physics*
306 *of the Earth and Planetary Interiors*, *27*(3), 194–205. https://doi.org/10.1016/0031-
307 9201(81)90016-9

308 Acocella, V. (2019). Bridging the Gap From Caldera Unrest to Resurgence. *Frontiers of Earth*
309 *Science in China*, *7*, 173. https://doi.org/10.3389/feart.2019.00173

310 Acocella, V., & Funiciello, R. (1999). The interaction between regional and local tectonics
311 during resurgent doming: the case of the island of Ischia, Italy. *Journal of Volcanology*
312 *and Geothermal Research*, *88*(1–2), 109–123. https://doi.org/10.1016/s0377-
313 0273(98)00109-7

314 Acocella, V., Cifelli, F., & Funiciello, R. (2001). The control of overburden thickness on
315 resurgent domes: insights from analogue models. *Journal of Volcanology and*
316 *Geothermal Research*, *111*(1–4), 137–153. https://doi.org/10.1016/s0377-
317 0273(01)00224-4

318 Acocella, V., Funiciello, R., Marotta, E., Orsi, G., & de Vita, S. (2004). The role of extensional
319 structures on experimental calderas and resurgence. *Journal of Volcanology and*
320 *Geothermal Research*, *129*(1), 199–217. https://doi.org/10.1016/S0377-0273(03)00240-
321 3

322 Acocella, V., Di Lorenzo, R., Newhall, C., & Scandone, R. (2015). An overview of recent
323 (1988 to 2014) caldera unrest: Knowledge and perspectives. *Reviews of Geophysics* ,
324 *53*(3), 896–955. https://doi.org/10.1002/2015rg000492

325 Aki, K., & Richards, P. G. (1980). *Quantitative seismology: theory and methods* (Vol. 842).
326 Freeman San Francisco, CA.

Amelung, F., Jónsson, S., Zebker, H., & Segall, P. (2000). Widespread uplift and 'trapdoor' faulting on Galápagos volcanoes observed with radar interferometry. *Nature*, *407*(6807), 993–996. https://doi.org/10.1038/35039604

Albuquerque Seismological Laboratory (ASL)/USGS. (1988). Global Seismograph Network - IRIS/USGS [Data set]. International Federation of Digital Seismograph Networks. https://doi.org/10.7914/SN/IU

Baba, T., Takahashi, N., Kaneda, Y., Ando, K., Matsuoka, D., & Kato, T. (2015). Parallel Implementation of Dispersive Tsunami Wave Modeling with a Nesting Algorithm for the 2011 Tohoku Tsunami. *Pure and Applied Geophysics*, *172*(12), 3455–3472. https://doi.org/10.1007/s00024-015-1049-2

Bell, A. F., La Femina, P. C., Ruiz, M., Amelung, F., Bagnardi, M., Bean, C. J., et al. (2021). Caldera resurgence during the 2018 eruption of Sierra Negra volcano, Galápagos Islands. *Nature Communications*, *12*(1), 1397. https://doi.org/10.1038/s41467-021-21596-4

Bell, A. F., Hernandez, S., La Femina, P. C., & Ruiz, M. C. (2021). Uplift and seismicity driven by magmatic inflation at Sierra Negra volcano, Galápagos islands. *Journal of Geophysical Research, [Solid Earth]*, *126*(7). https://doi.org/10.1029/2021jb022244

Brothelande, E., Peltier, A., Got, J.-L., Merle, O., Lardy, M., & Garaebiti, E. (2016). Constraints on the source of resurgent doming inferred from analogue and numerical modeling — Implications on the current feeding system of the Yenkahe dome–Yasur volcano complex (Vanuatu). *Journal of Volcanology and Geothermal Research*, *322*, 225–240. https://doi.org/10.1016/j.jvolgeores.2015.11.023

Cole, J. W., Milner, D. M., & Spinks, K. D. (2005). Calderas and caldera structures: a review. *Earth-Science Reviews*, *69*(1), 1–26. https://doi.org/10.1016/j.earscirev.2004.06.004

Dahlen, F. A., & Tromp, J. (1998). *Theoretical Global Seismology*. Princeton University Press. https://doi.org/10.1515/9780691216157

Doyle, A. C., Singleton, R. J., & Yaldwyn, J. C. (1979). Volcanic activity and recent uplift on Curtis and Cheeseman Islands, Kermadec Group, Southwest Pacific. *Journal of the Royal Society of New Zealand*, *9*(1), 123–140. https://doi.org/10.1080/03036758.1979.10418159

Duputel, Z., Rivera, L., Kanamori, H., & Hayes, G. (2012). W phase source inversion for moderate to large earthquakes (1990–2010). *Geophysical Journal International*, *189*(2), 1125–1147. https://doi.org/10.1111/j.1365-246X.2012.05419.x

Dziewonski, A. M., & Anderson, D. L. (1981). Preliminary reference Earth model. *Physics of the Earth and Planetary Interiors*, *25*(4), 297–356. https://doi.org/10.1016/0031-9201(81)90046-7

Ekström, G. (1994). Anomalous earthquakes on volcano ring-fault structures. *Earth and Planetary Science Letters*, *128*(3–4), 707–712. https://doi.org/10.1016/0012-821x(94)90184-8

Ekström, G., Nettles, M., & Dziewoński, A. M. (2012). The global CMT project 2004–2010: Centroid-moment tensors for 13,017 earthquakes. *Physics of the Earth and Planetary Interiors*, *200-201*, 1–9. https://doi.org/10.1016/j.pepi.2012.04.002

Fukao, Y., Sandanbata, O., Sugioka, H., Ito, A., Shiobara, H., Watada, S., & Satake, K. (2018). Mechanism of the 2015 volcanic tsunami earthquake near Torishima, Japan. *Science Advances*, *4*(4), eaao0219. https://doi.org/10.1126/sciadv.aao0219

Global Volcanism Program. (2013). Curtis Island (242010). In E. Venzke (Ed.), *Volcanoes of the World, v. 4.10.2 (24 Aug 2021)*. Smithsonian Institution. Retrieved from https://volcano.si.edu/volcano.cfm?vn=242010

Gregg, P. M., Le Mével, H., Zhan, Y., Dufek, J., Geist, D., & Chadwick, W. W., Jr. (2018). Stress triggering of the 2005 eruption of Sierra Negra volcano, Galápagos. *Geophysical Research Letters*, *45*(24), 13288–13297. https://doi.org/10.1029/2018gl080393

Gregg, P. M., Zhan, Y., Amelung, F., Geist, D., Mothes, P., Koric, S., & Yunjun, Z. (2022). Forecasting mechanical failure and the 26 June 2018 eruption of Sierra Negra Volcano, Galápagos, Ecuador. *Science Advances*, *8*(22), eabm4261. https://doi.org/10.1126/sciadv.abm4261

Gusman, A. R., Kaneko, Y., Power, W., & Burbidge, D. (2020). Source process for two enigmatic repeating vertical-T CLVD tsunami earthquakes in the kermadec ridge. *Geophysical Research Letters*, *47*(16). https://doi.org/10.1029/2020gl087805

Hanks, T. C., & Kanamori, H. (1979). A moment magnitude scale. *Journal of Geophysical Research*, *84*(B5), 2348. https://doi.org/10.1029/jb084ib05p02348

Hayes, G. P., Rivera, L., & Kanamori, H. (2009). Source Inversion of the W-Phase: Real-time Implementation and Extension to Low Magnitudes. *Seismological Research Letters*, *80*(5), 817–822. https://doi.org/10.1785/gssrl.80.5.817

Ho, T.-C., Satake, K., & Watada, S. (2017). Improved phase corrections for transoceanic tsunami data in spatial and temporal source estimation: Application to the 2011 Tohoku earthquake. *Journal of Geophysical Research, [Solid Earth]*, *122*(12), 10155–10175. https://doi.org/10.1002/2017jb015070

394 H., G., & Geoscience Australia. (2021). Australian National Seismograph Network Data
395 Collection [Data set]. Commonwealth of Australia (Geoscience Australia).
396 https://doi.org/10.26186/144675
397 Institut de physique du globe de Paris (IPGP), & École et Observatoire des Sciences de la Terre
398 de Strasbourg (EOST). (1982). GEOSCOPE, French Global Network of broad band
399 seismic stations [Data set]. Institut de physique du globe de Paris (IPGP), Université de
400 Paris. https://doi.org/10.18715/GEOSCOPE.G
401 Jónsson, S. (2009). Stress interaction between magma accumulation and trapdoor faulting on
402 Sierra Negra volcano, Galápagos. *Tectonophysics*, *471*(1), 36–44.
403 https://doi.org/10.1016/j.tecto.2008.08.005
404 Kajiura, K. (1963). The Leading Wave of a Tsunami. *Bulletin of the Earthquake Research*
405 *Institute, University of Tokyo*, *41*(3), 535–571. Retrieved from
406 https://ci.nii.ac.jp/naid/120000866529/
407 Kanamori, H. (1977). The energy release in great earthquakes. *Journal of Geophysical*
408 *Research*, *82*(20), 2981–2987. https://doi.org/10.1029/jb082i020p02981
409 Kanamori, H., & Given, J. W. (1981). Use of long-period surface waves for rapid
410 determination of earthquake-source parameters. *Physics of the Earth and Planetary*
411 *Interiors*, *27*(1), 8–31. https://doi.org/10.1016/0031-9201(81)90083-2
412 Kanamori, H., & Rivera, L. (2008). Source inversion of Wphase: speeding up seismic tsunami
413 warning. *Geophysical Journal International*, *175*(1), 222–238.
414 https://doi.org/10.1111/j.1365-246X.2008.03887.x
415 Kanamori, H., Ekström, G., Dziewonski, A., Barker, J. S., & Sipkin, S. A. (1993). Seismic
416 radiation by magma injection: An anomalous seismic event near Tori Shima, Japan.

Journal of Geophysical Research, *98*(B4), 6511–6522. https://doi.org/10.1029/92jb02867

Kawakatsu, H. (1996). Observability of the isotropic component of a moment tensor. *Geophysical Journal International*, *126*(2), 525–544. https://doi.org/10.1111/j.1365-246X.1996.tb05308.x

Kawakatsu, H., & Yamamoto, M. (2015). 4.15 - Volcano Seismology. In G. Schubert (Ed.), *Treatise on Geophysics (Second Edition)* (pp. 389–419). Oxford: Elsevier. https://doi.org/10.1016/B978-0-444-53802-4.00081-6

Molin, P., Acocella, V., & Funiciello, R. (2003). Structural, seismic and hydrothermal features at the border of an active intermittent resurgent block: Ischia Island (Italy). *Journal of Volcanology and Geothermal Research*, *121*(1–2), 65–81. https://doi.org/10.1016/s0377-0273(02)00412-2

Nikkhoo, M., & Walter, T. R. (2015). Triangular dislocation: an analytical, artefact-free solution. *Geophysical Journal International*, *201*(2), 1119–1141. https://doi.org/10.1093/gji/ggv035

Peregrine, D. H. (1972). Equations for Water Waves and the Approximation behind Them. In R. E. Meyer (Ed.), *Waves on Beaches and Resulting Sediment Transport* (pp. 95–121). Academic Press. https://doi.org/10.1016/B978-0-12-493250-0.50007-2

Persson, P.-O., & Strang, G. (2004). A Simple Mesh Generator in MATLAB. *SIAM Review. Society for Industrial and Applied Mathematics*, *46*(2), 329–345. https://doi.org/10.1137/s0036144503429121

Sandanbata, O., Watada, S., Satake, K., Fukao, Y., Sugioka, H., Ito, A., & Shiobara, H. (2018). Ray Tracing for Dispersive Tsunamis and Source Amplitude Estimation Based on

Green's Law: Application to the 2015 Volcanic Tsunami Earthquake Near Torishima, South of Japan. *Pure and Applied Geophysics*, *175*(4), 1371–1385. https://doi.org/10.1007/s00024-017-1746-0

Sandanbata, O., Kanamori, H., Rivera, L., Zhan, Z., Watada, S., & Satake, K. (2021). Moment tensors of ring-faulting at active volcanoes: Insights into vertical-CLVD earthquakes at the Sierra Negra caldera, Galápagos islands. *Journal of Geophysical Research, [Solid Earth]*, *126*(6), e2021JB021693. https://doi.org/10.1029/2021jb021693

Sandanbata, O., Watada, S., Ho, T.-C., & Satake, K. (2021). Phase delay of short-period tsunamis in the density-stratified compressible ocean over the elastic Earth. *Geophysical Journal International*, *226*(3), 1975–1985. https://doi.org/10.1093/gji/ggab192

Sandanbata, O., Watada, S., Satake, K., Kanamori, H., Rivera, L., & Zhan, Z. (2022, February 14). *Sub-decadal Volcanic Tsunamis Due to Submarine Trapdoor Faulting at Sumisu Caldera in the Izu-Bonin Arc*. *Earth and Space Science Open Archive*. https://doi.org/10.1002/essoar.10510526.3

Satake, K., & Kanamori, H. (1991). Abnormal tsunamis caused by the June 13, 1984, Torishima, Japan, earthquake. *Journal of Geophysical Research*, *96*(B12), 19933–19939. https://doi.org/10.1029/91jb01903

Shuler, A., Nettles, M., & Ekström, G. (2013). Global observation of vertical-CLVD earthquakes at active volcanoes. *Journal of Geophysical Research, [Solid Earth]*, *118*(1), 138–164. https://doi.org/10.1029/2012jb009721

461 Shuler, A., Ekström, G., & Nettles, M. (2013). Physical mechanisms for vertical-CLVD
462 earthquakes at active volcanoes. *Journal of Geophysical Research, [Solid Earth]*,
463 *118*(4), 1569–1586. https://doi.org/10.1002/jgrb.50131
464 Silver, P. G., & Jordan, T. H. (1982). Optimal estimation of scalar seismic moment.
465 *Geophysical Journal International*, *70*(3), 755–787. https://doi.org/10.1111/j.1365-
466 246X.1982.tb05982.x
467 Takeuchi, H., & Saito, M. (1972). Seismic surface waves. *Methods in Computational Physics*,
468 *11*, 217–295.
469 Watada, S., Kusumoto, S., & Satake, K. (2014). Traveltime delay and initial phase reversal of
470 distant tsunamis coupled with the self-gravitating elastic Earth. *Journal of Geophysical*
471 *Research, [Solid Earth]*, *119*(5), 4287–4310. https://doi.org/10.1002/2013jb010841
472 Weatherall, P., Marks, K. M., & Jakobsson, M. (2015). A new digital bathymetric model of the
473 world's oceans. *Earth and Space*. https://doi.org/10.1002/2015EA000107
474 Wells, D. L., & Coppersmith, K. J. (1994). New Empirical Relationships among Magnitude,
475 Rupture Length, Rupture Width, Rupture Area, and Surface Displacement. *Bulletin of*
476 *the Seismological Society of America*, *84*(4), 974–1002.
477 https://doi.org/10.1785/BSSA0840040974
478 Zheng, Y., Blackstone, L., & Segall, P. (2022). Constraints on absolute magma chamber
479 volume from geodetic measurements of trapdoor faulting at Sierra Negra volcano,
480 Galapagos. *Geophysical Research Letters*, *49*(5). https://doi.org/10.1029/2021gl095683

481
482

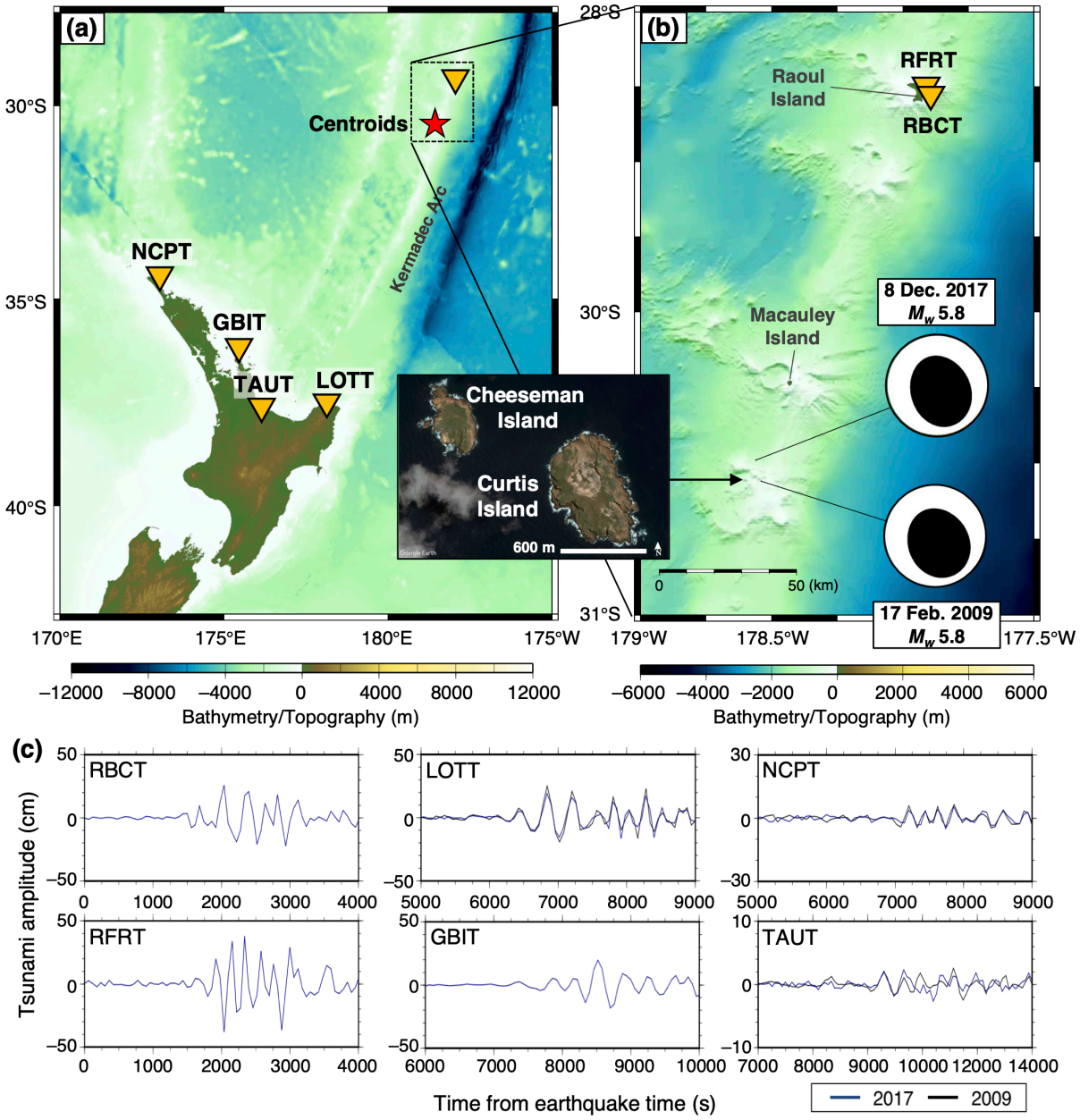

Figure 1. The Curtis earthquakes. (**a**–**b**) Earthquake centroids (red star) and tide gauges (triangles). The inset figure shows a satellite image of the islands obtained from Google Earth. (**c**) Tsunami waveforms of tige gauges. Black and blue lines represent waveforms from the 2009 and 2017 earthquakes, respectively.

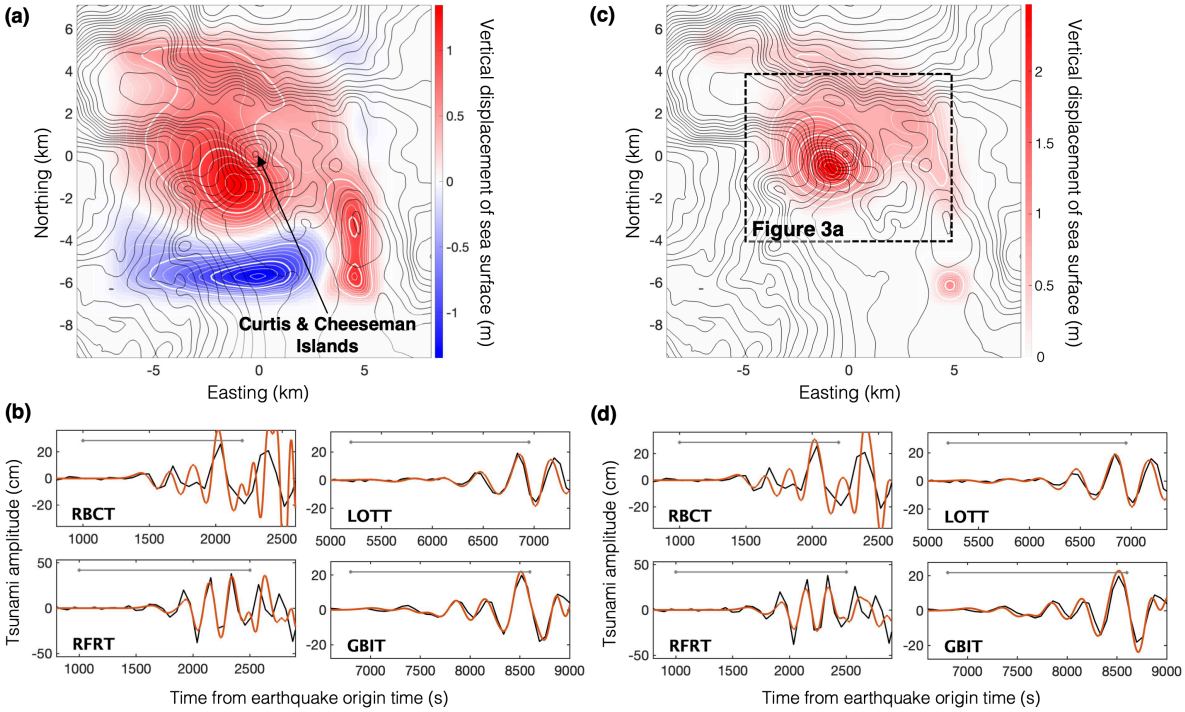

Figure 2. Vertical sea-surface displacement models. (**a**) Model estimated when uplift and subsidence are allowed, and (**b**) its synthetic waveforms (red), compared with observation (black) (**c**) Model estimated when only uplift is allowed, and (**d**) its synthetic waveforms. In **a** and **c**, black contour lines are plotted every 50 m of water depth. In **b** and **d**, gray lines represent data lengths for the inversion. The rectangle in **c** indicates the area shown in Figure 3a.

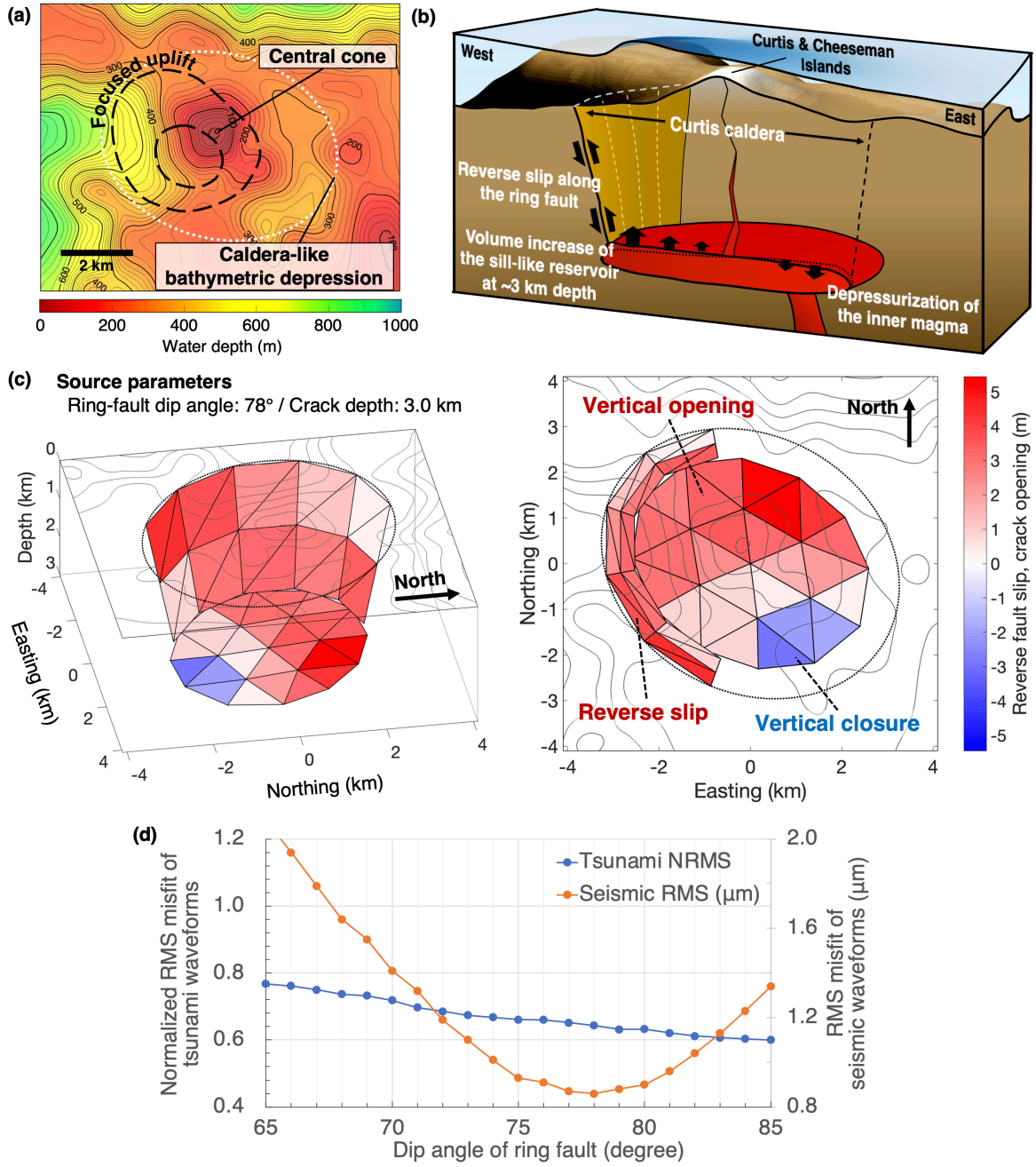

Figure 3. Trapdoor faulting mechanism of the 2017 Curtis earthquake. (**a**) Bathymetry near the islands. Black dashed lines represent 1-m and 2-m contours of the sea-surface uplift model (Figure 2c). (**b**) Schematic illustration of the mechanism (not scaled). (**c**) Our best-fit source model. Red color on the ring fault represents reverse slip. Red and blue colors on the horizontal crack represent vertical opening and closing, respectively. (a) Tsunami and seismic waveform misfits for models with different dip angles.

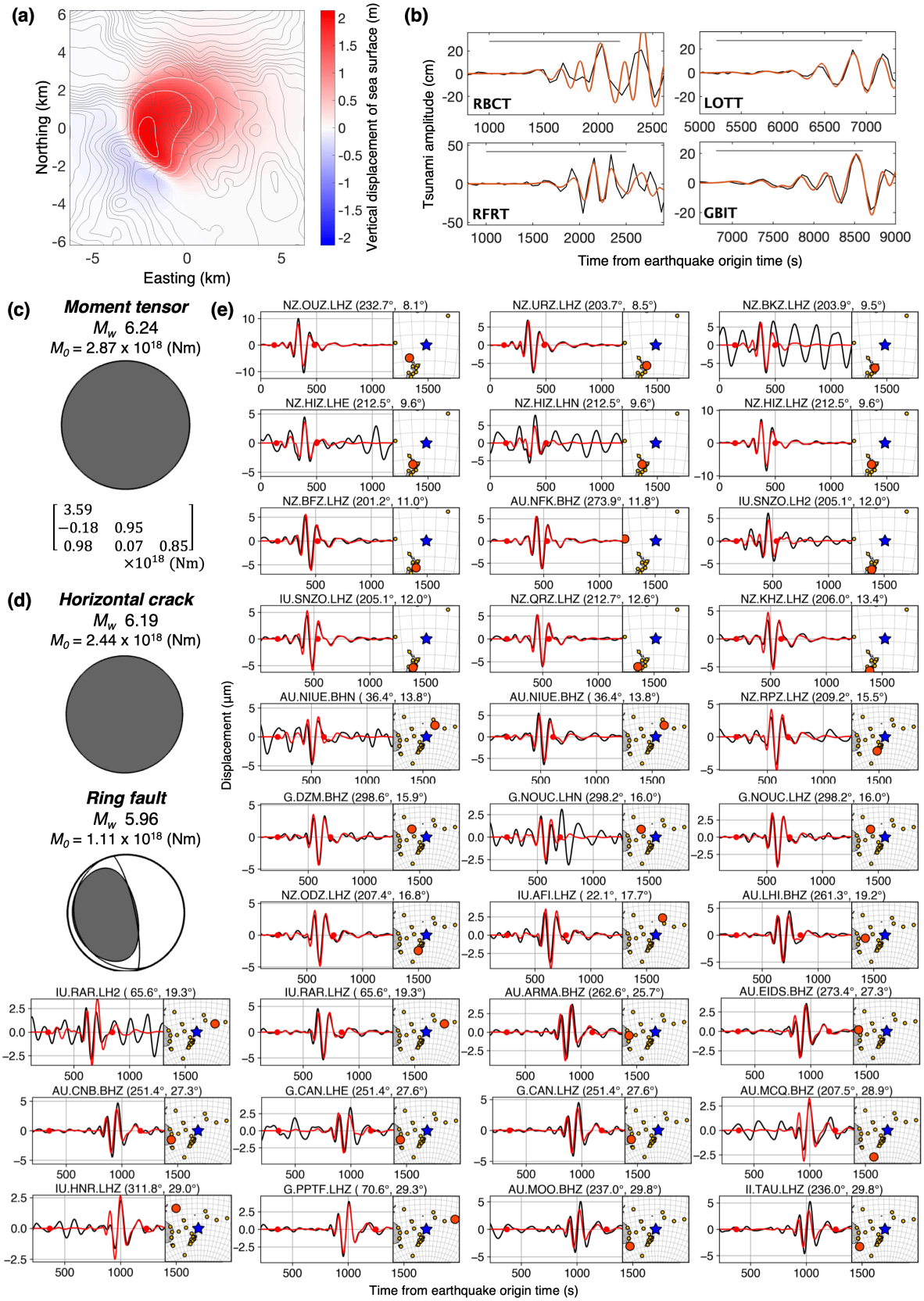
(a)
Northing (km)
Easting (km)
Vertical displacement of sea surface (m)
(b)
Tsunami amplitude (cm)
RBCT
LOTT
RFRT
GBIT
Time from earthquake origin time (s)
(c)
Moment tensor
M_w 6.24
M_0 = 2.87 x 10^{18} (Nm)
3.59
−0.18 0.95
0.98 0.07 0.85
×10^{18} (Nm)
(d)
Horizontal crack
M_w 6.19
M_0 = 2.44 x 10^{18} (Nm)
Ring fault
M_w 5.96
M_0 = 1.11 x 10^{18} (Nm)
(e)
Displacement (μm)
NZ.OUZ.LHZ (232.7°, 8.1°)
NZ.URZ.LHZ (203.7°, 8.5°)
NZ.BKZ.LHZ (203.9°, 9.5°)
NZ.HIZ.LHE (212.5°, 9.6°)
NZ.HIZ.LHN (212.5°, 9.6°)
NZ.HIZ.LHZ (212.5°, 9.6°)
NZ.BFZ.LHZ (201.2°, 11.0°)
AU.NFK.BHZ (273.9°, 11.8°)
IU.SNZO.LH2 (205.1°, 12.0°)
IU.SNZO.LHZ (205.1°, 12.0°)
NZ.QRZ.LHZ (212.7°, 12.6°)
NZ.KHZ.LHZ (206.0°, 13.4°)
AU.NIUE.BHN (36.4°, 13.8°)
AU.NIUE.BHZ (36.4°, 13.8°)
NZ.RPZ.LHZ (209.2°, 15.5°)
G.DZM.BHZ (298.6°, 15.9°)
G.NOUC.LHN (298.2°, 16.0°)
G.NOUC.LHZ (298.2°, 16.0°)
NZ.ODZ.LHZ (207.4°, 16.8°)
IU.AFI.LHZ (22.1°, 17.7°)
AU.LHI.BHZ (261.3°, 19.2°)
IU.RAR.LH2 (65.6°, 19.3°)
IU.RAR.LHZ (65.6°, 19.3°)
AU.ARMA.BHZ (262.6°, 25.7°)
AU.EIDS.BHZ (273.4°, 27.3°)
AU.CNB.BHZ (251.4°, 27.3°)
G.CAN.LHE (251.4°, 27.6°)
G.CAN.LHZ (251.4°, 27.6°)
AU.MCQ.BHZ (207.5°, 28.9°)
IU.HNR.LHZ (311.8°, 29.0°)
G.PPTF.LHZ (70.6°, 29.3°)
AU.MOO.BHZ (237.0°, 29.8°)
II.TAU.LHZ (236.0°, 29.8°)
Time from earthquake origin time (s)

505

506 **Figure 4**. Model performance of the best-fit source model (Figure 3c). (**a**) Vertical sea-surface
507 displacement. (**b**) Synthetic (red) and observed (black) tsunami waveforms. Gray lines
508 represent data lengths used for the inversion. (**c**) Moment tensor of the model. (**d**) Partial
509 moment tensors of the horizontal crack and the ring fault. (**e**) Synthetic long-period
510 seismograms from the model (red; moment tensor in **c**) and observed seismograms (black). Red
511 dots delimitate the data length to calculate the waveform misfit. In inset figures, red circle and
512 blue star represent the station and the earthquake centroid, respectively. The network and
513 station names, record component, station azimuth and epicentral distance are indicated on top
514 of each panel.
515

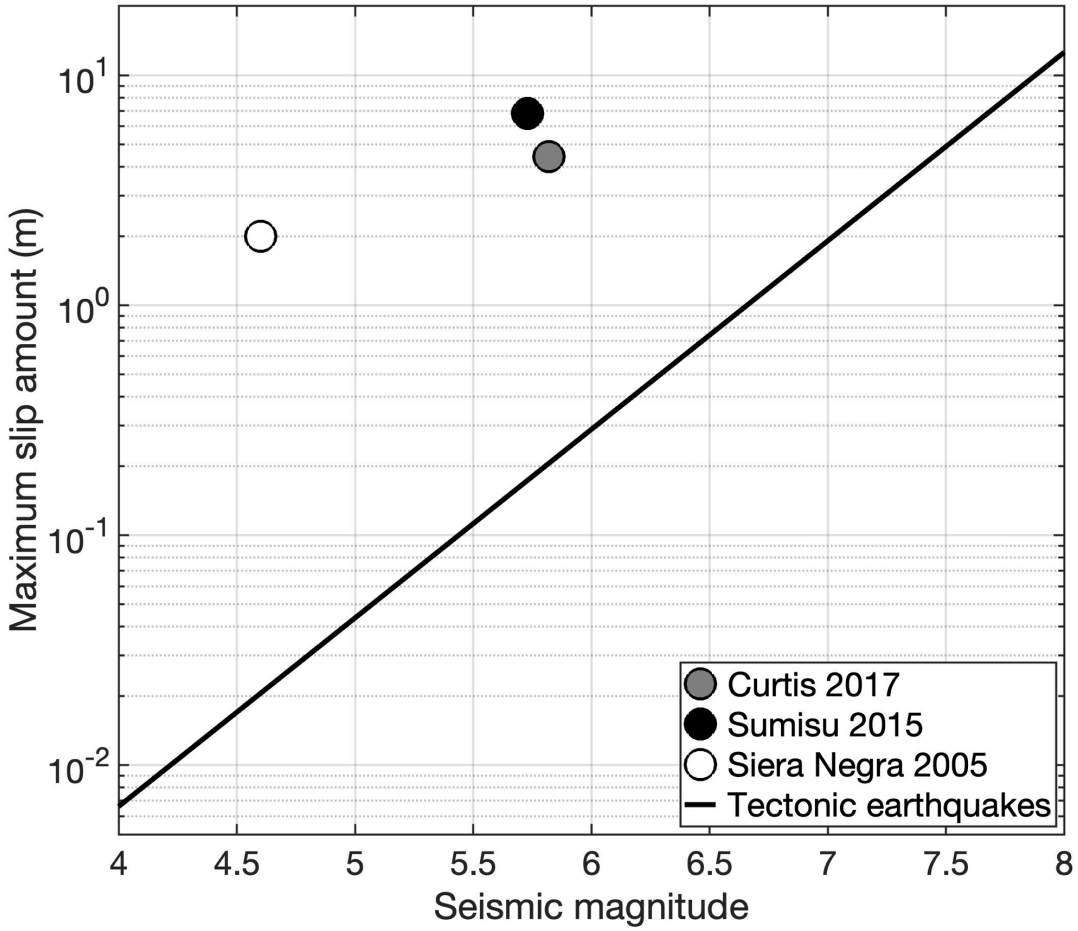

516

517 **Figure 5**. Scaling relationships of trapdoor faulting. Circles represent the maximum slip
518 amount and the seismic magnitude estimated for trapdoor faulting at Curtis (2017; this study),
519 Sumisu (2015; Sandanbata et al., 2022), and Sierra Negra calderas (2005; Zheng et al., 2022).
520 Black line represents the relationships for tectonic earthquakes (Wells & Coppersmith, 1994).

Geophysical Research Letter

Supporting Information for

Two volcanic tsunami events caused by trapdoor faulting at a submerged caldera near Curtis and Cheeseman Islands in the Kermadec Arc

Osamu Sandanbata[1,2,†], Shingo Watada[1], Kenji Satake[1], Hiroo Kanamori[3], and Luis Rivera[4]

[1]Earthquake Research Institute, the University of Tokyo, Tokyo, Japan.

[2]National Research Institute for Earth Science and Disaster Resilience, Ibaraki, Japan.

[3]Seismological Laboratory, California Institute of Technology, Pasadena, CA, USA.

[4]Université de Strasbourg, CNRS, ITES UMR 7063, Strasbourg F-67084, France.

Contents of this file

Additional Supporting Information (Files uploaded separately)

Caption for Data Set S1

Introduction

In this supporting information, we describe methodologies for estimation of the vertical sea-surface displacement (Text S1), earthquake source modeling (Text S2), moment tensor representation of our source model (Text S3), and moment tensor analysis (Text S4). We also include supplementary figures and tables to support the conclusion stated in Main Text. In Data Set S1, we contain the data of the best-fit source model of the 2017 earthquake.

Text S1 Methodology for estimation of the vertical sea-surface displacement

We estimate the vertical sea-surface displacement of the 2017 Curtis earthquake using a tsunami inversion method. We set a tsunami source area of 25 km × 25 km square around Curtis and Cheeseman Islands and distribute 181 unit sources of vertical sea-surface displacement with 1.25 km intervals (Figure S8), each of which is formulated as:

$$\eta^k(x,y) = 0.25 \times \left[1.0 + \cos\frac{\pi(x-x^k)}{L}\right] \times \left[1.0 + \cos\frac{\pi(y-y^k)}{L}\right], \quad \left(|x-x^k|, |y-y^k| \le L\right) \tag{S1}$$

where η^k is the vertical sea-surface displacement (in meter) of the k-th unit source ($k = 1, \dots, K$; here $K = 181$) with the central location at (x^k, y^k) (in km) with a source size of L (1.25 km, here).

We compute the Green's function $\boldsymbol{g} = g_j^k$, relating the k-th unit source to tsunami waveform at the j-th station ($j = 1, \dots, J$; here $J = 4$). We use the simulation code JAGURS (Baba et al., 2015) to solve the standard Boussinesq-type equations (Peregrine, 1972). The rise time for each unit source is assumed as 10 s, which is similar to a source duration of 6 s determined by the moment tensor analysis (see Text S4; Table S2). Bathymetry data in broad regions is modeled with GEBCO_2014 (Weatherall et al., 2015) with 30 arcsec grid spacing, and the New Zealand Regional Bathymetry with 250 m grid spacing downloaded from the National Institute of Water and Atmospheric Research (NIWA) in New Zealand. To include nearshore effects around tide gauges, we use finer bathymetry data (~28 m) obtained by combining digital topographic data on land and bathymetric data digitized and interpolated from analogue charts of the Land Information of New Zealand (LINZ) department. Tsunami speed is reduced by the elasticity of the Earth, the compressibility and the density stratification of seawater, and the gravitational potential change due to tsunami motions, (Ho et al., 2017; Sandanbata, Watada, et al., 2021; Watada et al., 2014). Sandanbata, Watada, et al. (2021) expected that short-period tsunamis with a period of 500 s in water of 1-km depth are delayed by about 3 s every 100-km distance. Hence, to approximately incorporate the delay effect, we delay the synthetic waveforms by 25 s at LOTT and GBIT with epicentral distances of ~830 km.

We then solve the observation equation by the damped least-squares method (pp. 695–699 in Aki & Richards [1980]):

$$\begin{bmatrix} \boldsymbol{d} \\ \boldsymbol{0} \end{bmatrix} = \begin{bmatrix} \boldsymbol{g} \\ \alpha \boldsymbol{I} \end{bmatrix} \boldsymbol{m}, \tag{S2}$$

where $\boldsymbol{d} = [d_1(t) \quad \dots \quad d_J(t)]^T$ is the column vector of the observed tsunami data at the j-th station, $\boldsymbol{g} = \begin{bmatrix} g_1^1(t) & \cdots & g_1^K(t) \\ \vdots & \ddots & \vdots \\ g_J^1(t) & \cdots & g_J^K(t) \end{bmatrix}$ is the Green's function, $\boldsymbol{m} = [m^1 \quad \dots \quad m^K]^T$ is an unknown column vector of the amplitude factor of the k-th unit source, $\boldsymbol{I}$ is the identity matrix, and α is the damping parameter to obtain a smooth source model, which we assume as 0.02. We set data length to include several wave crests and troughs of the

tsunami signal. By the superposition of the unit sources η^k weighted by m_i^k, we obtain the vertical sea-surface displacement model. Additionally, we obtain uplift source model without subsidence, by solving Equation S2 with the non-negative condition (i.e., $\boldsymbol{m} \geq \mathbf{0}$).

Text S2 Methodology for earthquake source modeling

S2.1 Source structures of the fault-crack composite source system

We assume a fault-crack composite source system, composed of an inward-dipping ring fault connected to a horizontal crack at a depth of 3 km, which is discretized with triangular meshes (Figure S1). Given the focused uplift estimated in Section 3 in Main Text, we assume a partial ring fault on the southwestern side of the caldera that extends from seafloor to the crack edge. The ring fault is along an elliptical line; this ellipse is with the center at (178.56°W, 30.542°S), the major axis oriented S60°E, and the horizontal size of 3.4 km × 2.8 km on the seafloor. For the ring fault, we assume a uniform inward dip angle, varied from 65° to 85°. Only inward dip angles are considered, because the vertical-T CLVD moment tensor can be generated when the caldera floor uplifts along with an inward ring fault (see Figure 1 in Sandanbata, Kanamori, et al. 2021; Figure 9 in Shuler, Ekström, et al., 2013). Thus, we prepare tens of source structures with different ring-fault dip angles.

We discretize the source system into triangular source elements. The ring fault is divided into elements with an arc angle of 30° along the circumference and 1.5 km along the depth, and a trapezoid composed of two neighboring triangular elements with the same dip and strike angles is considered as a sub-fault. The horizontal crack is discretized using the DistMesh code (Persson & Strang, 2004), each of which is considered as sub-crack. By a tsunami waveform inversion explained later, we will determine amounts of the reverse slip of each sub-fault and the opening/closure of each sub-crack, denoted by $\boldsymbol{s} = [s_1 \quad \cdots \quad s_{N_s}]^T$ and $\boldsymbol{\delta} = [\delta_1 \quad \cdots \quad \delta_{N_\delta}]^T$, respectively. Because the dislocations of the ring fault and the horizontal crack should be similar to each other at their contacts, we link the vertical component of the sub-fault slip at bottom to the sub-crack opening/closing at edge adjacent to the sub-fault by imposing a kinematic condition:

$$s_p \sin \Delta_p = \delta_q \tag{S3}$$

where Δ_p is the dip angle of the p-th sub-fault to which the q-th sub-crack is adjacent.

S2.2 Tsunami waveform inversion of fault-crack composite source models

For each source structure assumed above, we perform a tsunami waveform inversion to obtain a fault-crack composite source model. We use the same tsunami data, as described in Section 2.1 of Main Text.

To efficiently compute the Green's function relating each sub-fault slip or sub-crack opening to the tsunami waveforms, we use the method proposed in a previous study (Sandanbata et al., 2022), which is summarized as follows. First, we compute the vertical sea-surface displacement excited by unit dislocation of the i-th source element (i.e., 1-m reverse slip of sub-fault or 1-m vertical opening of sub-crack; $i = 1, \ldots, I$; here I depend

on source structure). We calculate vertical *seafloor* displacement due to each source element by the triangular dislocation method (Nikkhoo & Walter, 2015) assuming flat seafloor and Poisson's ratio of 0.25, and we convert it into vertical *sea-surface* displacement by applying the Kajiura's filter (Kajiura, 1963). The water depth of 400 m is used for this filter. We thus compute the sea-surface displacement from the i-th source element $h_i(x, y)$. Second, we approximate the vertical sea-surface displacement $h_i(x, y)$ of the i-th source element by a linear combination of the unit sources $\eta^k(x, y)$ used in Section 3 of Main Text and Text S1 (Equation S1; Figure S8):

$$h_i(x, y) \approx \sum_{k=1}^{K} m_i^k \eta^k(x, y), \tag{S4}$$

where the amplitude factors m_i^k are obtained by a least-squares method. Third, we compute the Green's functions relating the i-th source element to the tsunami data at the j-th station by superimposing the Green's functions of the unit sources g_j^k multiplied by the amplitude factors m_i^k:

$$G_{ij}(t) = \sum_k m_i^k g_j^k(t). \tag{S5}$$

Finally, to obtain a source model, we determine the motions of the fault-crack composite source system by solving the observation equation with the damped least-squares method:

$$\begin{bmatrix} \boldsymbol{d} \\ \boldsymbol{0} \\ \boldsymbol{0} \end{bmatrix} = \begin{bmatrix} \boldsymbol{G} \\ \boldsymbol{K} \\ \beta \boldsymbol{I} \end{bmatrix} \begin{bmatrix} \boldsymbol{s} \\ \boldsymbol{\delta} \end{bmatrix}, \tag{S6}$$

where $\boldsymbol{d}$ is the observed tsunami data at the j-th station, and $\boldsymbol{G} = \begin{bmatrix} G_{11}(t) & \cdots & G_{I1}(t) \\ \vdots & \ddots & \vdots \\ G_{1J}(t) & \cdots & G_{IJ}(t) \end{bmatrix}$ is the matrix of the Green's functions G_{ij}. $\boldsymbol{s}$ is an unknown column vector of reverse slip amounts for sub-faults, for which we impose the non-zero condition ($\boldsymbol{s} \geq \boldsymbol{0}$), and $\boldsymbol{\delta}$ is an unknown column vector of opening amounts for sub-cracks, for which we allow either positive (opening) or negative (closing) values. The linear equation of $\boldsymbol{K} \begin{bmatrix} \boldsymbol{s} \\ \boldsymbol{\delta} \end{bmatrix} = \boldsymbol{0}$ represents the kinematic condition of Equation S3. β is the damping parameter, which we set at 0.015 by taking a balance between the solution smoothness and the waveform fit (Figure S9).

To evaluate the waveform fit between the observed tsunami waveforms and synthetic waveforms from an obtained source model, we quantify the normalized root-mean-square (NRMS) misfit of the tsunami waveforms, which we call *tsunami NRMS misfit*:

$$\sqrt{\sum_j \left\| \boldsymbol{c}_j^t - \boldsymbol{d}_j^t \right\|^2 / \sum_j \left\| \boldsymbol{c}_j^t \right\|^2}, \tag{S7}$$

where $\boldsymbol{c}_j^t$ and $\boldsymbol{d}_j^t$ are the observed waveform and synthetic waveforms within the inversion time window at the j-th station, respectively. $\| \ \|$ denotes the L2 norm of data vector.

S.2.3 Forward computation of long-period seismic waveforms

For validation of fault-crack composite source models obtained by the tsunami waveform inversion, we compute long-period seismic waveforms from the source models and compare them with the seismic data. The moment tensor of the models $\boldsymbol{M}$ is written by:

$$\boldsymbol{M} = \boldsymbol{M}_{RF} + \boldsymbol{M}_{HC} = \sum \boldsymbol{m}_{RF}^{p} + \sum \boldsymbol{m}_{HC}^{q}, \tag{S8}$$

where $\boldsymbol{M}_{RF}$ and $\boldsymbol{M}_{HC}$ represent moment tensors of the ring fault and the horizontal crack, respectively, and $\boldsymbol{m}_{RF}^{p}$ and $\boldsymbol{m}_{HC}^{q}$ are moment tensors of the p-th sub-fault and the q-th sub-crack, respectively. We compute $\boldsymbol{m}_{RF}^{p}$ with the slip amount and strike, dip, and rake (90°) angles (Box 4.4 in Aki & Richards, 1980), with the seismic moment of $\mu s_p A_p$, where s_p and A_p are slip amount and area, respectively, and μ is rigidity, or Lamé's constant. We calculate $\boldsymbol{m}_{HC}^{q}$ by:

$$\boldsymbol{m}_{HC}^{q} = \begin{bmatrix} M_{rr} & M_{\theta r} & M_{\phi r} \\ M_{r\theta} & M_{\theta\theta} & M_{\phi\theta} \\ M_{r\phi} & M_{\theta\phi} & M_{\phi\phi} \end{bmatrix} = \delta_q \times A_q \times \begin{bmatrix} \lambda + 2\mu & 0 & 0 \\ 0 & \lambda & 0 \\ 0 & 0 & \lambda \end{bmatrix}, \tag{S9}$$

where δ_q and A_q are the opening amount and area, respectively (Kawakatsu & Yamamoto, 2015). We assume Lamé's constants of λ and μ as 34.2 GPa, and 26.6 GPa, respectively, calculated with the P- and S-wave velocities and the density in the shallowest crust layer of 1-D Preliminary Reference Earth Model (PREM) (Dziewonski & Anderson, 1981). The total seismic moment is calculated by

$$M_0 = \sqrt{\Sigma_{ij} M_{ij} M_{ij} / 2}, \tag{S10}$$

(pp. 166–167 in Dahlen & Tromp, 1998; Silver & Jordan, 1982) and the moment magnitude by

$$M_w = \frac{2}{3}(\log_{10} M_0 - 9.10), \tag{S11}$$

with M_0 in the N m scale (Hanks & Kanamori, 1979; Kanamori, 1977).

Using the W-phase package (Duputel et al., 2012; Hayes et al., 2009; Kanamori & Rivera, 2008), we compute long-period seismic waveforms from the moment tensor $\boldsymbol{M}$. Green's functions of seismic waves are calculated with the PREM model by the normal mode method (Takeuchi & Saito, 1972). The centroid is at the center of Curtis caldera (178.56°W, 30.54°S) and at the depth of 0.5 km below the seafloor. Both the half duration and the centroid time shift are assumed to be 5 s, which are comparable to the values (3 s and 3 s) obtained by the moment tensor inversion (Text S4; Table S2). We apply the same filter to the synthetic waveforms, as used for the seismic data.

To quantify the seismic waveform fit, we calculate the root-mean-square (RMS) misfit of the seismic waveforms, which we call *seismic RMS misfit*:

$$\sqrt{\sum_j \left\| \boldsymbol{c}_j^{\boldsymbol{s}} - \boldsymbol{d}_j^{\boldsymbol{s}} \right\|^2}, \tag{S12}$$

where $\boldsymbol{c}_j^s$ and $\boldsymbol{d}_j^s$ are the synthetic and observed seismic waveforms at the j-th record. The data length for this calculation includes P, S, and surface waves.

Text S3 Contribution to long-period seismic waves

The moment tensor of our best-fit source model $\boldsymbol{M}$ is highly isotropic with M_w 6.24 (Figure 4c), whereas the deviatoric moment tensor of the 2017 Curtis earthquake reported in the GCMT catalogue is a vertical-T CLVD type with M_w 5.8 (Figure 1b). Here we discuss the reason for the differences between the moment tensors. Figure S6a shows synthetic seismograms at representative stations from the moment tensor $\boldsymbol{M}$ (= $\boldsymbol{M_{HC}}$ + $\boldsymbol{M_{RF}}$) of our model. For comparison, we show synthetic seismograms from moment tensors of the horizontal crack $\boldsymbol{M_{HC}}$ and the ring fault $\boldsymbol{M_{RF}}$ in Figures S6b and S6c, respectively. Although $\boldsymbol{M_{HC}}$ has a larger moment magnitude (M_w 6.19) than $\boldsymbol{M_{RF}}$ (M_w 5.96), the seismic amplitudes from $\boldsymbol{M_{HC}}$ are much smaller than those from $\boldsymbol{M_{RF}}$. This is because the vertical motion of a horizontal crack at a very shallow depth has only a low efficiency of long-period seismic radiation (Fukao et al., 2018; Sandanbata, Kanamori, et al., 2021). Note that the polarities of seismograms from $\boldsymbol{M_{HC}}$ are reversed to those from $\boldsymbol{M_{RF}}$, which is known as the trade-off between the vertical-CLVD and isotropic components at shallow depth (Kawakatsu, 1996; Sandanbata, Kanamori, et al., 2021; compare Figures S6b and S6c). Hence, $\boldsymbol{M_{HC}}$ slightly reduces the seismic amplitudes from $\boldsymbol{M}$ but does not change the waveform shapes much.

To further examine radiations from the ring fault, we show in Figure S6d synthetic seismograms from $\boldsymbol{M_{RF}}$ excluding two elements representing vertical dip-slip, $M_{r\theta}$ and $M_{r\varphi}$ (i.e., from M_{rr}, $M_{\theta\theta}$, $M_{\varphi\varphi}$, and $M_{\theta\varphi}$ of $\boldsymbol{M_{RF}}$). Although the moment magnitude decreases by 0.2 compared to that of $\boldsymbol{M_{RF}}$, the synthetic seismograms are very similar to those from $\boldsymbol{M_{RF}}$. This demonstrates that the two excluded elements, $M_{r\theta}$ and $M_{r\varphi}$, at a very shallow depth are very inefficient in radiating long-period seismic waves (Sandanbata, Kanamori, et al., 2021). Hence, long-period seismic waves of the earthquakes mainly arise from the four elements, M_{rr}, $M_{\theta\theta}$, $M_{\varphi\varphi}$, and $M_{\theta\varphi}$, of $\boldsymbol{M_{RF}}$. This moment tensor composed of the four elements is a vertical-T CLVD type, which is very similar to the GCMT solution (Figure 1b).

Text S4 Moment tensor analysis

We use the W-phase code (Duputel et al., 2012; Hayes et al., 2009; Kanamori & Rivera, 2008) to perform the deviatoric moment tensor (MT) inversion analysis for the 2009 and 2017 earthquakes using long-period seismic data. This analysis is independent of the source modeling in Main Text. For the two earthquakes, we download seismic records of LH and BH channels at stations within 5°–30° from different seismic networks (network codes: II, IU, AU, NZ, and G). For computation of the Green's function of seismic waveforms, we use the normal mode method (Takeuchi & Saito, 1972) with the 1-D Preliminary Reference Earth Model (PREM) (Dziewonski & Anderson, 1981). The time window includes P, S, and surface waves. We impose the zero-trace constraint, $M_{rr} + M_{\theta\theta} + M_{\varphi\varphi} = 0$. We assume the centroid location at (178.56°W, 30.54°S) and the depth at 2.5 km in the crust, and apply the same filter, as done in the source modeling (see Text S2.3). We start the inversion with a half duration t_h and a centroid time shift t_c reported in

the GCMT catalog, and grid-search optimal values for t_h = t_c. During the inversion process, we select seismic data yielding a single-record normalized root-mean-square (NRMS) misfit ≤ 1.0, which is calculated by $\sqrt{\|\boldsymbol{c}_i^s - \boldsymbol{d}_i^s\| / \|\boldsymbol{c}_i^s\|}$, where $\boldsymbol{c}_i^s$ and $\boldsymbol{d}_i^s$ are synthetic and observed data in the inversion window at the i-th station, respectively. The selected datasets are composed of 29 and 33 records of the 2009 and 2017 earthquakes, respectively (Figures S10 and S11).

Table S2 shows the obtained deviatoric moment tensor of the 2009 and 2017 earthquakes. The seismic moment and moment magnitude of the two earthquakes are much larger than those in the GCMT catalogue (Table S1), because for such shallow earthquakes $M_{r\theta}$ and $M_{r\varphi}$ cannot be estimated accurately (Kanamori & Given, 1981; Sandanbata, Kanamori, et al., 2021).

Following a previous study (Sandanbata, Kanamori, et al., 2021), we estimate the ring-fault geometries of the 2009 and 2017 earthquakes using *resolvable moment tensor* $\boldsymbol{M_{res}}$. We obtain $\boldsymbol{M_{res}}$ by removing $M_{r\theta}$ and $M_{r\varphi}$ from the estimated deviatoric moment tensor, decompose $\boldsymbol{M_{res}}$ into two components, i.e., vertical-CLVD component $\boldsymbol{M_{CLVD}}$ and vertical strike-slip component $\boldsymbol{M_{SS}}$, and calculate the moment ratio of $\boldsymbol{M_{CLVD}}$ to $\boldsymbol{M_{SS}}$, or the CLVD ratio k_{CLVD}. Figure S7 shows thus-obtained $\boldsymbol{M_{res}}$ and the CLVD ratios of the two earthquakes. Using the relationships between the Null-axis direction of $\boldsymbol{M_{res}}$ and the ring-fault orientation, and between k_{CLVD} and the arc angle of the ring fault (see Figure 4 in Sandanbata, Kanamori, et al., 2021), we estimate that the 2009 and 2017 earthquakes occurred with ring faults with arc angles of ~100° and ~120°, respectively, both of which are oriented in the NNW–SSW direction.

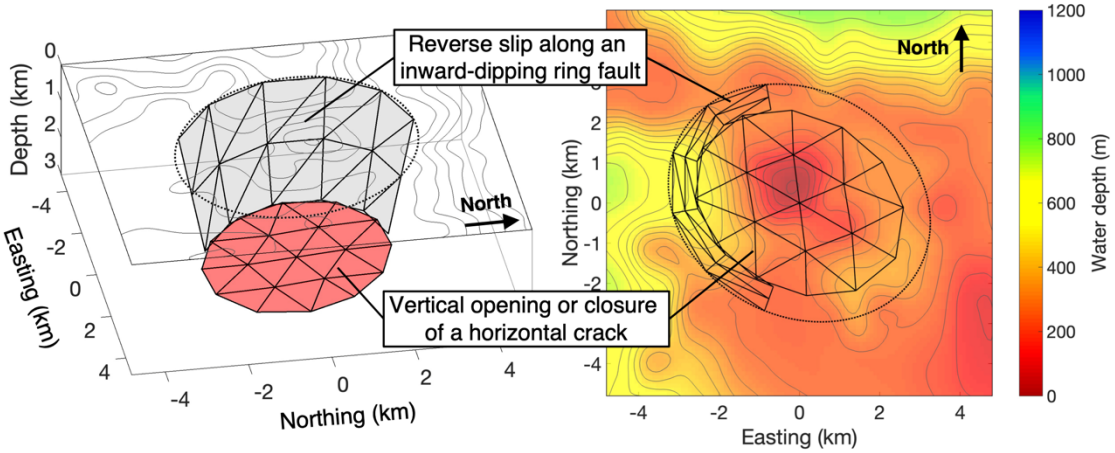

Figure S1. An assumed fault-crack composite source system, composed of a partial ring fault and a horizontal crack, viewed from the east (left) and above (right). This structure is discretized into triangular meshes.

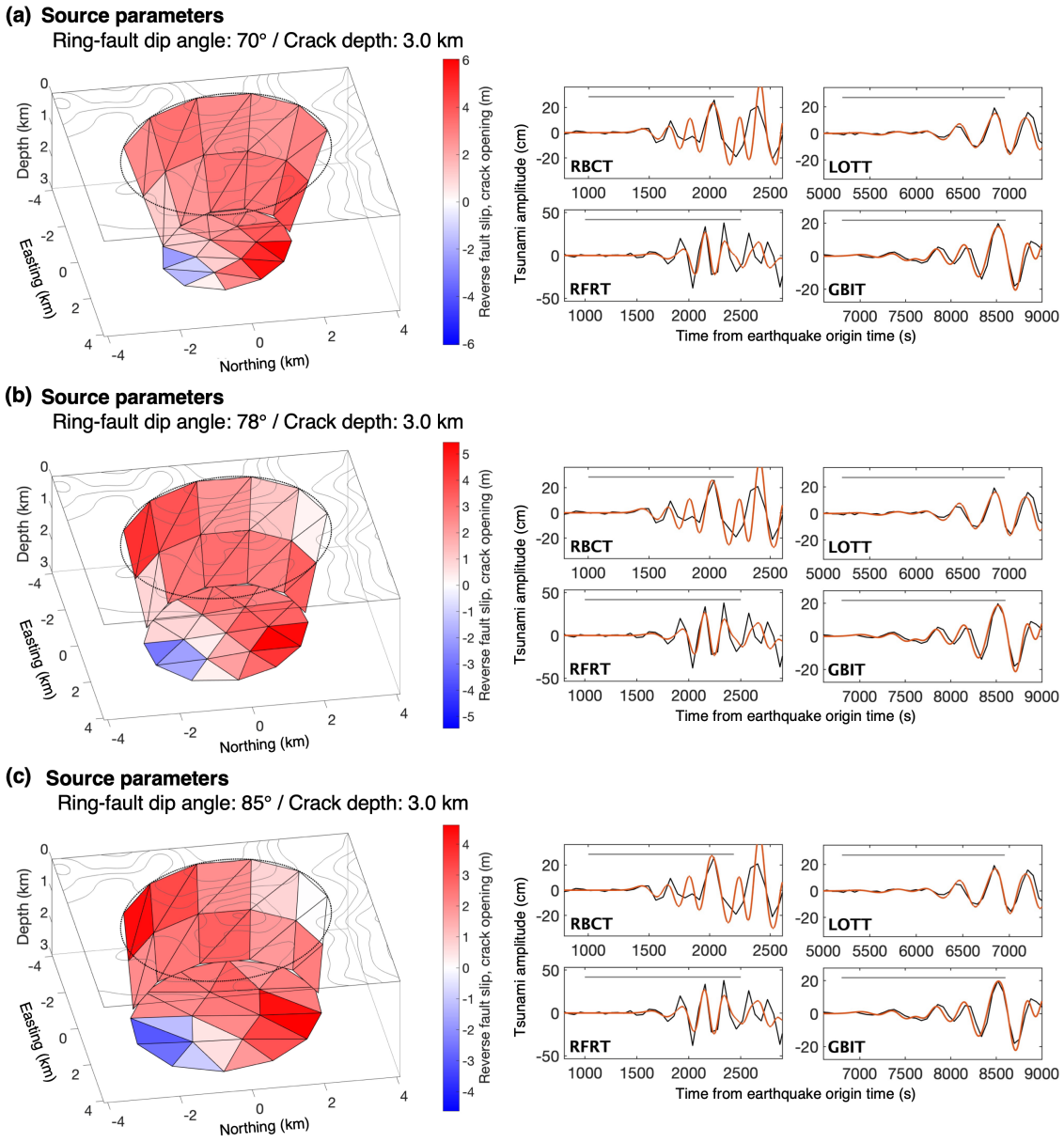

Figure S2. Source models with different ring-fault dip angle: (**a**) 70°, (**b**) 78°, and (**c**) 85°. All the models have a horizontal crack at a depth of 3 km. (Left) The fault-crack motion determined by the tsunami waveform inversion. See the caption of Figure 3c. (Right) Synthetic tsunami waveforms from this model (red), compared with observed waveforms (black). See the caption of Figure 4b. Note that variations of the ring-fault dip angle do not change the tsunami waveforms.

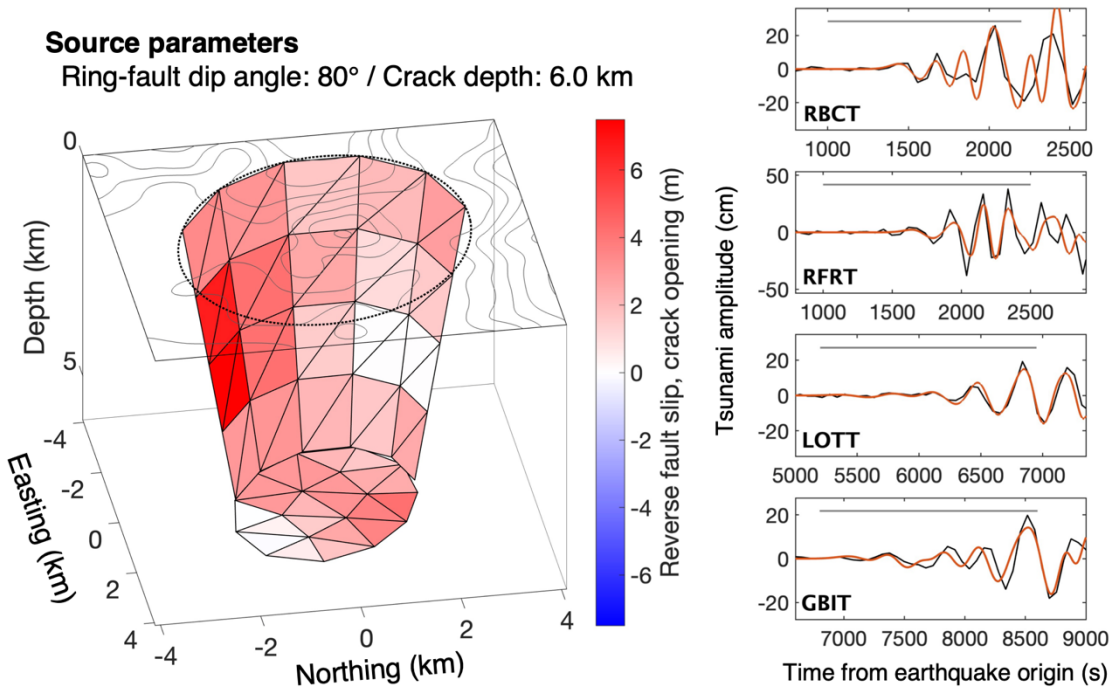

Figure S3. Source model with a horizontal crack at a depth of 6 km. (Left) The fault-crack motion determined by the tsunami waveform inversion. See the caption of Figure 3c. (Right) Synthetic tsunami waveforms from this model (red), compared with observed waveforms (black). See the caption of Figure 4b.

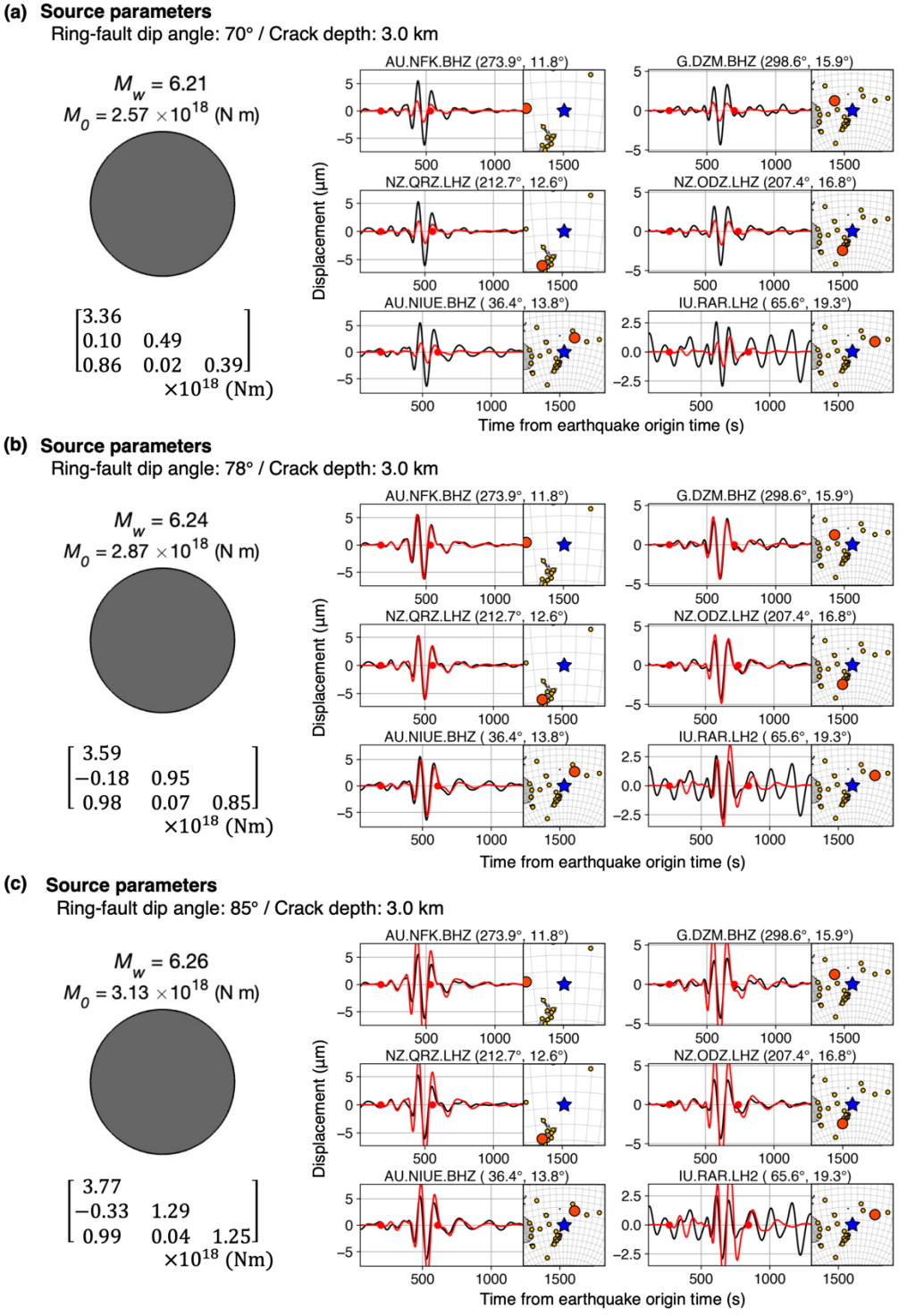

Figure S4. Moment tensor and seismic waveforms from the source models with a dip angle of (**a**) 70°, (**b**) 78°, and (**c**) 85°; all these models have a horizontal crack at 3 km depth, which are shown in Figure S3. Red and black lines represent synthetic and observed waveforms, respectively. Note that variations of the ring-fault dip angle change the seismic wave amplitudes largely.

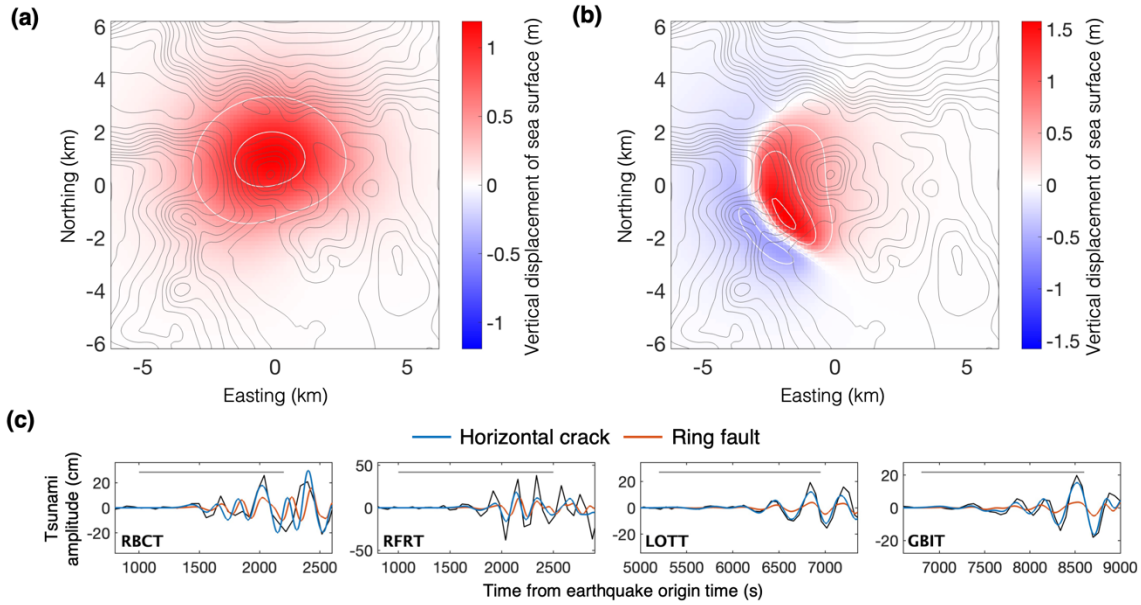

Figure S5. Partial contributions of the horizontal crack and the ring fault of the best-fit source model (Figure 3c) to the tsunami waveforms. (**a**–**b**) Vertical sea-surface displacements caused by (**a**) the horizontal crack and (**b**) the ring fault. Red and blue colors represent uplift and subsidence, respectively, with white contour lines plotted every 0.5 m. (**c**) Comparison of the synthetic tsunami waveforms from the horizontal crack (blue) and the ring fault (red), compared with the observed (black) waveforms. The gray line represents the time interval used for the inversion.

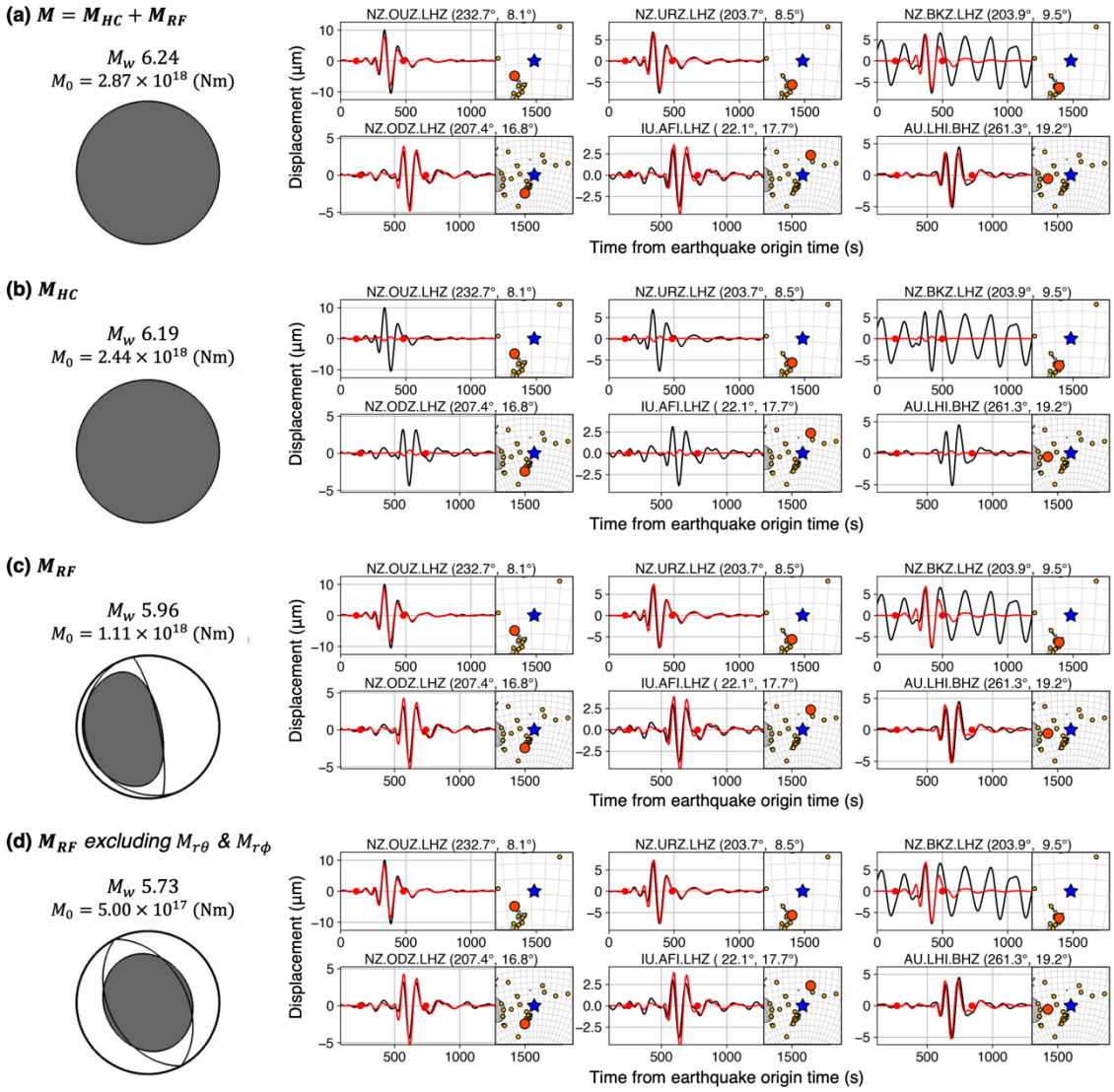

Figure S6. Contributions of the best-fit source model (Figure 3c) to long-period seismic waves. Red lines in the right panels represent synthetic waveforms from (**a**) $\boldsymbol{M}$ (= $\boldsymbol{M_{HC}}$ + $\boldsymbol{M_{RF}}$), the partial moment tensors of (**b**) the horizontal crack $\boldsymbol{M_{HC}}$ and (**c**) the ring fault $\boldsymbol{M_{RF}}$, and (**d**) the moment tensor of the ring fault, excluding $M_{r\theta}$ and $M_{r\varphi}$. Note that that the smaller-amplitude waveforms from $\boldsymbol{M_{HC}}$ have the reversed polarities to those from $\boldsymbol{M_{RF}}$, reducing the seismic amplitudes of $\boldsymbol{M}$, and that the main contributor to the long-period seismic waves is the limited moment-tensor components shown in **d**.

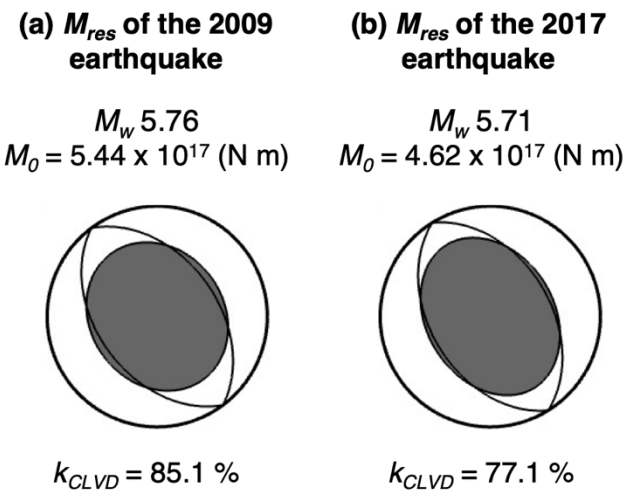

Figure S7. Resolvable moment tensors $\boldsymbol{M_{res}}$ of the (**a**) 2017 and (**b**) 2009 Curtis earthquakes determined by the moment tensor analysis (see Text S4). The orientation of the best double-couple solution is shown by thin curves, whose Null-axis direction coincides with that of $\boldsymbol{M_{res}}$. The focal mechanisms are shown by projection of the lower focal hemisphere.

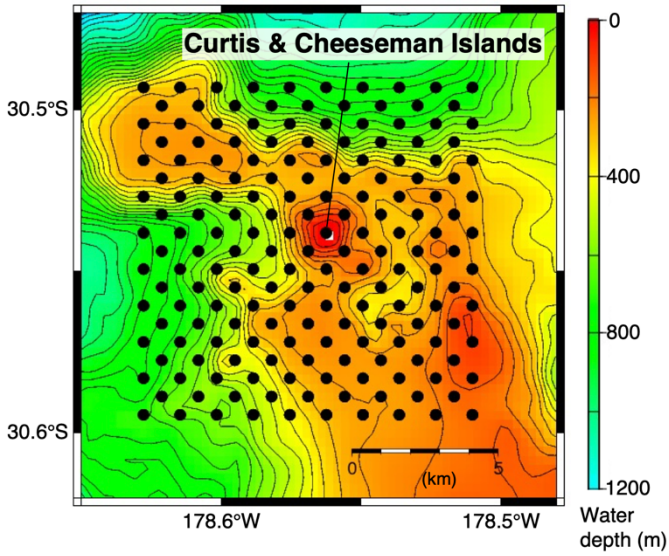

Figure S8. Unit sources of initial sea-surface displacement around Curtis & Cheeseman Islands. Black dots represent central locations of the unit sources. Each unit source has a cosine-tapered shape with a horizontal source size of 1.25 km x 1.25 km. Contour lines of the water depth are plotted every 50 m.

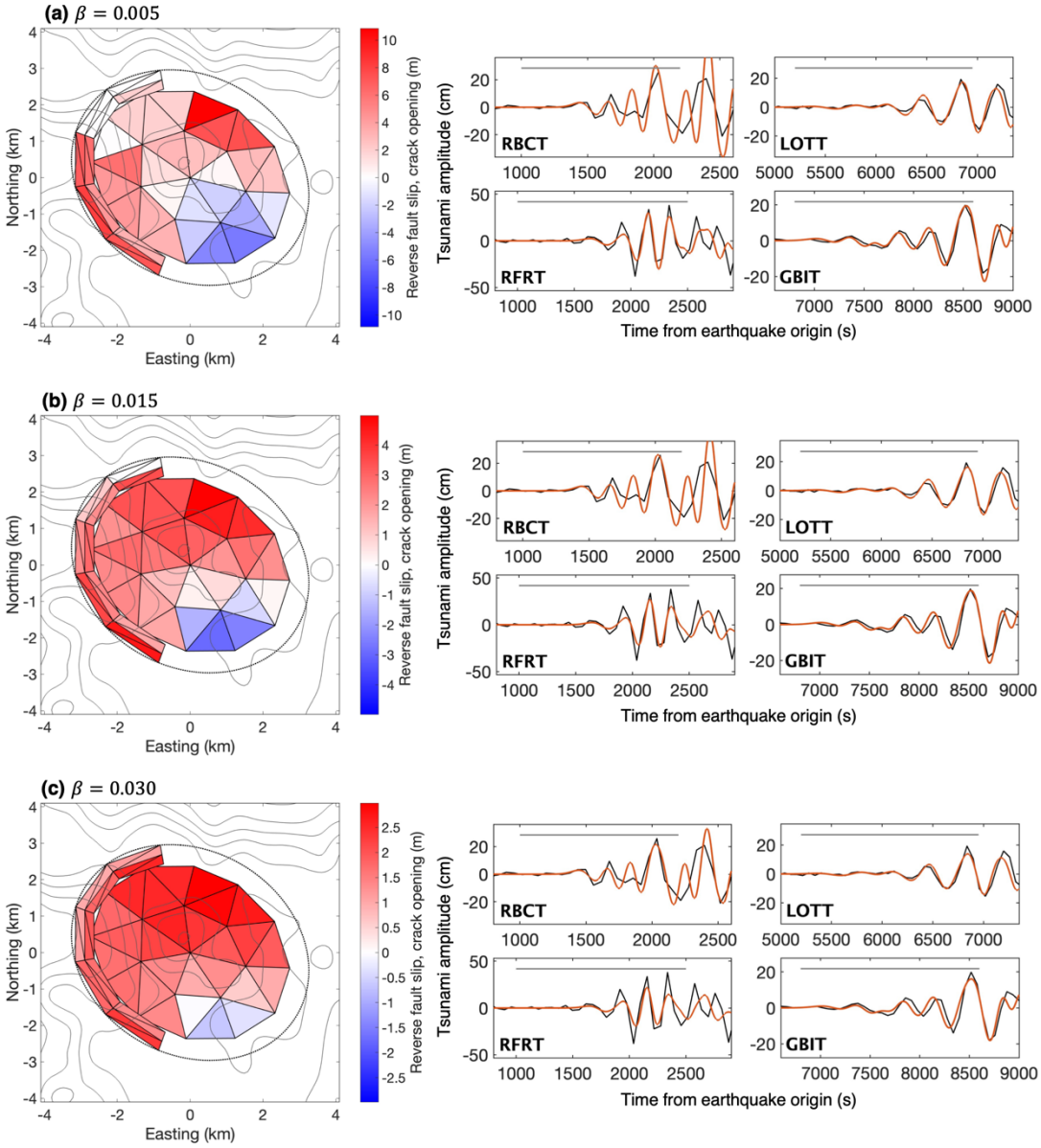

Figure S9. Source models inverted with different damping parameters $\boldsymbol{\beta}$ of (**a**) 0.005, (**b**) 0.015, and (**c**) 0.030. (Left) Fault-crack motions inverted by the tsunami inversion. See captions of Figure 3c. (Right) Synthetic tsunami waveforms from the models (red), compared with observed waveforms (black). See the caption of Figure 4b. By taking the balance between the solution smoothness and the tsunami waveform fit, we use $\boldsymbol{\beta}$ of 0.015.

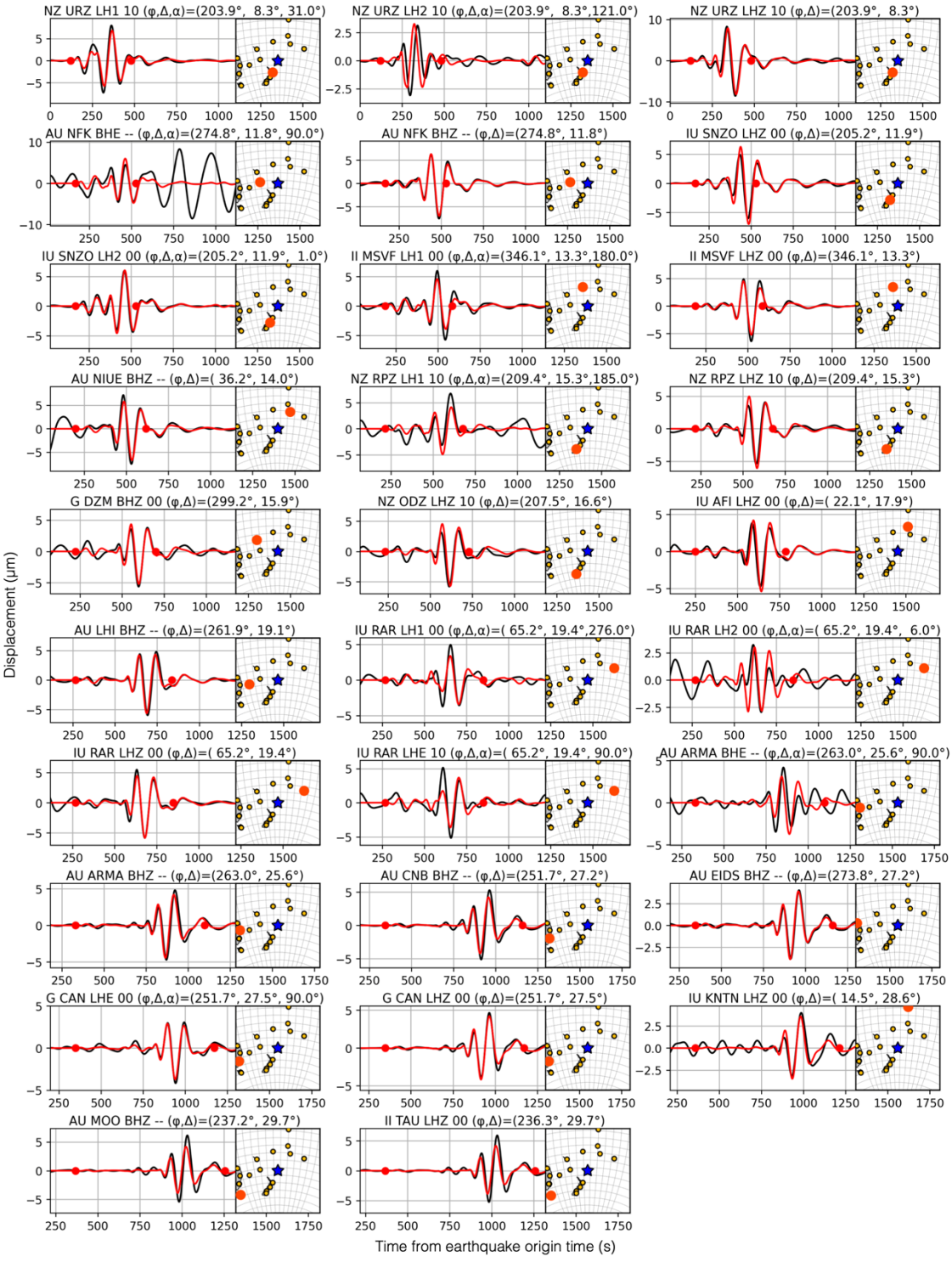

Figure S10. Model performance of the MT analysis for the 2009 earthquake. Red and black lines represent synthetic and observed waveforms, respectively. The time window for the inversion is indicated by red dots.

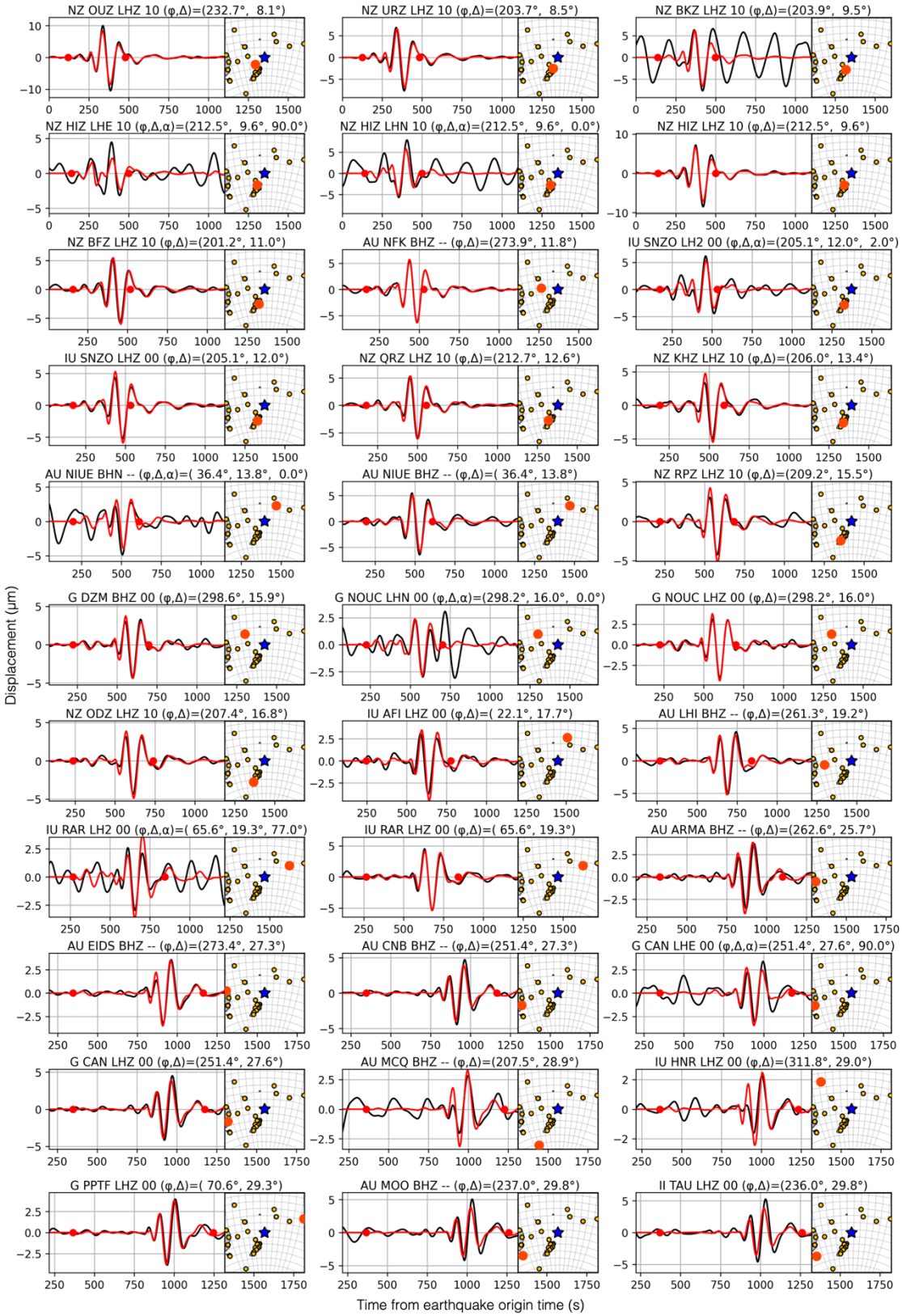

Figure S11. Same as Figure S10, but for the 2017 earthquake.

Date	Time	Longitude	Latitude	Depth	M_w	M_s
17 Feb. 2009	03:30:58.6	178.54°W	30.56°S	12.1 km	5.8	6.0
8 Dec. 2017	02:10:03.0	178.56°W	30.49°S	13.4 km	5.8	6.2

Table S1. Earthquake information reported in the GCMT catalogue. Note that the depth may be determined at a greater depth than the accurate depth to maintain the stability of solutions (Ekström et al., 2012).

Event	M_w	M_0 (10^{18} N m)	Moment tensor (10^{18} N m)						t_s (s)
			M_{rr}	$M_{\theta\theta}$	$M_{\phi\phi}$	$M_{r\theta}$	$M_{r\phi}$	$M_{\theta\phi}$	
2009	6.45	5.92	0.615	-0.276	-0.339	-2.201	-5.468	0.103	4.0
2017	6.45	5.98	0.505	-0.186	-0.320	-2.441	-5.437	0.134	3.0

Table S2. Deviatoric moment tensor inversion results for the 2009 and 2017 earthquakes using long-period seismic data. We assume that the centroid time shift t_c and the half duration t_h are the same. Note that two elements representing the vertical dip-slip ($M_{r\theta}$ and $M_{r\varphi}$) are poorly determined because of their weak excitation of long-period seismic waves (Kanamori & Given, 1981; Sandanbata, Kanamori, et al., 2021).

Moment tensor	M_w	M_0 (10^{18} N m)	Moment tensor (10^{18} N m)					
			M_{rr}	$M_{\theta\theta}$	$M_{\varphi\varphi}$	$M_{r\theta}$	$M_{r\varphi}$	$M_{\theta\varphi}$
Composite, $\boldsymbol{M}$	6.24	2.87	3.59	0.95	0.85	-0.18	0.98	0.07
Horizontal crack, $\boldsymbol{M}_{HC}$	6.19	2.44	3.02	1.18	1.18	0.00	0.00	0.00
Ring-fault, $\boldsymbol{M}_{RF}$	5.96	1.11	0.57	-0.23	-0.34	-0.18	0.98	0.07

Table S3. Moment tensors of our best-fit source model (Figure 3c) of the 2017 earthquake: the moment tensor of the model $\boldsymbol{M}$ (**= $\boldsymbol{M_{HC}}$ + $\boldsymbol{M_{RF}}$**), and the partial moment tensors of the horizontal crack $\boldsymbol{M_{HC}}$ and the ring fault $\boldsymbol{M_{RF}}$.

Data Set S1. Fault-crack composite source model (separate file). This dataset includes four models presented in Figure 3c.

References

Aki, K., & Richards, P. G. (1980). *Quantitative seismology: theory and methods* (Vol. 842). Freeman San Francisco, CA.

Baba, T., Takahashi, N., Kaneda, Y., Ando, K., Matsuoka, D., & Kato, T. (2015). Parallel Implementation of Dispersive Tsunami Wave Modeling with a Nesting Algorithm for the 2011 Tohoku Tsunami. *Pure and Applied Geophysics*, *172*(12), 3455–3472. https://doi.org/10.1007/s00024-015-1049-2

Dahlen, F. A., & Tromp, J. (1998). *Theoretical Global Seismology*. Princeton University Press. https://doi.org/10.1515/9780691216157

Duputel, Z., Rivera, L., Kanamori, H., & Hayes, G. (2012). W phase source inversion for moderate to large earthquakes (1990–2010). *Geophysical Journal International*, *189*(2), 1125–1147. https://doi.org/10.1111/j.1365-246X.2012.05419.x

Dziewonski, A. M., & Anderson, D. L. (1981). Preliminary reference Earth model. *Physics of the Earth and Planetary Interiors*, *25*(4), 297–356. https://doi.org/10.1016/0031-9201(81)90046-7

Ekström, G., Nettles, M., & Dziewoński, A. M. (2012). The global CMT project 2004–2010: Centroid-moment tensors for 13,017 earthquakes. *Physics of the Earth and Planetary Interiors*, *200-201*, 1–9. https://doi.org/10.1016/j.pepi.2012.04.002

Fukao, Y., Sandanbata, O., Sugioka, H., Ito, A., Shiobara, H., Watada, S., & Satake, K. (2018). Mechanism of the 2015 volcanic tsunami earthquake near Torishima, Japan. *Science Advances*, *4*(4), eaao0219. https://doi.org/10.1126/sciadv.aao0219

Hanks, T. C., & Kanamori, H. (1979). A moment magnitude scale. *Journal of Geophysical Research*, *84*(B5), 2348. https://doi.org/10.1029/jb084ib05p02348

Hayes, G. P., Rivera, L., & Kanamori, H. (2009). Source Inversion of the W-Phase: Real-time Implementation and Extension to Low Magnitudes. *Seismological Research Letters*, *80*(5), 817–822. https://doi.org/10.1785/gssrl.80.5.817

Ho, T.-C., Satake, K., & Watada, S. (2017). Improved phase corrections for transoceanic tsunami data in spatial and temporal source estimation: Application to the 2011 Tohoku earthquake. *Journal of Geophysical Research, [Solid Earth]*, *122*(12), 10155–10175. https://doi.org/10.1002/2017jb015070

Kajiura, K. (1963). The Leading Wave of a Tsunami. *Bulletin of the Earthquake Research Institute, University of Tokyo*, *41*(3), 535–571. Retrieved from https://ci.nii.ac.jp/naid/120000866529/

Kanamori, H. (1977). The energy release in great earthquakes. *Journal of Geophysical Research*, *82*(20), 2981–2987. https://doi.org/10.1029/jb082i020p02981

Kanamori, H., & Given, J. W. (1981). Use of long-period surface waves for rapid determination of earthquake-source parameters. *Physics of the Earth and Planetary Interiors*, *27*(1), 8–31. https://doi.org/10.1016/0031-9201(81)90083-2

Kanamori, H., & Rivera, L. (2008). Source inversion of Wphase: speeding up seismic tsunami warning. *Geophysical Journal International*, *175*(1), 222–238. https://doi.org/10.1111/j.1365-246X.2008.03887.x

Kawakatsu, H. (1996). Observability of the isotropic component of a moment tensor. *Geophysical Journal International*, *126*(2), 525–544. https://doi.org/10.1111/j.1365-246X.1996.tb05308.x

Kawakatsu, H., & Yamamoto, M. (2015). 4.15 - Volcano Seismology. In G. Schubert (Ed.), *Treatise on Geophysics (Second Edition)* (pp. 389–419). Oxford: Elsevier. https://doi.org/10.1016/B978-0-444-53802-4.00081-6

Nikkhoo, M., & Walter, T. R. (2015). Triangular dislocation: an analytical, artefact-free solution. *Geophysical Journal International*, *201*(2), 1119–1141. https://doi.org/10.1093/gji/ggv035

Peregrine, D. H. (1972). Equations for Water Waves and the Approximation behind Them. In R. E. Meyer (Ed.), *Waves on Beaches and Resulting Sediment Transport* (pp. 95–121). Academic Press. https://doi.org/10.1016/B978-0-12-493250-0.50007-2

Persson, P.-O., & Strang, G. (2004). A Simple Mesh Generator in MATLAB. *SIAM Review*. *Society for Industrial and Applied Mathematics*, *46*(2), 329–345. https://doi.org/10.1137/s0036144503429121

Sandanbata, O., Kanamori, H., Rivera, L., Zhan, Z., Watada, S., & Satake, K. (2021). Moment tensors of ring-faulting at active volcanoes: Insights into vertical-CLVD earthquakes at the Sierra Negra caldera, Galápagos islands. *Journal of Geophysical Research, [Solid Earth]*, *126*(6), e2021JB021693. https://doi.org/10.1029/2021jb021693

Sandanbata, O., Watada, S., Ho, T.-C., & Satake, K. (2021). Phase delay of short-period tsunamis in the density-stratified compressible ocean over the elastic Earth. *Geophysical Journal International*, *226*(3), 1975–1985. https://doi.org/10.1093/gji/ggab192

Sandanbata, O., Watada, S., Satake, K., Kanamori, H., Rivera, L., & Zhan, Z. (2022, February 14). *Sub-decadal Volcanic Tsunamis Due to Submarine Trapdoor Faulting at Sumisu Caldera in the Izu-Bonin Arc*. *Earth and Space Science Open Archive*. https://doi.org/10.1002/essoar.10510526.3

Shuler, A., Ekström, G., & Nettles, M. (2013). Physical mechanisms for vertical-CLVD earthquakes at active volcanoes. *Journal of Geophysical Research, [Solid Earth]*, *118*(4), 1569–1586. https://doi.org/10.1002/jgrb.50131

Silver, P. G., & Jordan, T. H. (1982). Optimal estimation of scalar seismic moment. *Geophysical Journal International*, *70*(3), 755–787. https://doi.org/10.1111/j.1365-246X.1982.tb05982.x

Takeuchi, H., & Saito, M. (1972). Seismic surface waves. *Methods in Computational Physics*, *11*, 217–295.

Watada, S., Kusumoto, S., & Satake, K. (2014). Traveltime delay and initial phase reversal of distant tsunamis coupled with the self-gravitating elastic Earth. *Journal of Geophysical Research, [Solid Earth]*, *119*(5), 4287–4310. https://doi.org/10.1002/2013jb010841

Weatherall, P., Marks, K. M., & Jakobsson, M. (2015). A new digital bathymetric model of the world's oceans. *Earth and Space*. https://doi.org/10.1002/2015EA000107